1 An empirical algorithm to seamlessly retrieve the

2 concentration of suspended particulate matter from water

3 color across ocean to turbid river mouths

4

5 Xiaolong Yu[1, 2, 3*], Zhongping Lee[1], Fang Shen[3], Menghua Wang[4], Jianwei Wei[4], Lide Jiang[4],

6 Zhehai Shang[1]

7 [1] University of Massachusetts Boston, School for the Environment, Boston, MA 02125, USA

8 [2] State Key Laboratory of Marine Environmental Science, College of Ocean and Earth Sciences,
9 Xiamen University, Xiamen, 361101, China

10 [3] State Key Laboratory of Estuarine and Coastal Research, East China Normal University, Shanghai,
11 200062, China

12 [4] NOAA National Environmental Satellite, Data, and Information Service, Center for Satellite
13 Applications and Research, E/RA3, 5830 University Research Court, College Park, MD 20740, USA

14 *corresponding author: xiaolong.yu@umb.edu

15

16 **Abstract:**

17   We propose a globally applicable algorithm (GAA$_{SPM}$) to seamlessly retrieve the

18 concentration of suspended particulate matter (SPM) (C_{SPM}) from remote sensing reflectance

19 ($R_{rs}(\lambda)$) across ocean to turbid river mouths without any hard-switching in its application.

20 GAA$_{SPM}$ is based on a calibrated relationship between C_{SPM} and a generalized index for SPM

21 (GI_{SPM}) from water color. The GI_{SPM} is mainly composed of three $R_{rs}(\lambda)$ ratios (671, 745, and

22 862 nm over 551 nm, respectively), along with weighting factors assigned to each ratio. The

23 weighting factors are introduced to ensure the progressive application of $R_{rs}(\lambda)$ in the longer

24 wavelengths for increasing C_{SPM}. Calibration of GAA$_{SPM}$ employed data collected from

25 multiple estuarine and coastal regions of Europe, China, Argentina, and the USA with the

26 measured C_{SPM} spanning from 0.2 to 2068.8 mg/L. Inter-comparison with several recalibrated

27 well-known C_{SPM} retrieval algorithms demonstrates that GAA$_{SPM}$ has the best retrieval

28 accuracy over the entire C_{SPM} range with a relative mean absolute difference (rMAD) of 41.3%

29 (N = 437). This averaged uncertainty in GAA$_{SPM}$-derived C_{SPM} is mostly attributed to the

30 retrievals from less turbid waters where C_{SPM} < 50 mg/L (rMAD = 50%, N = 214). GAA$_{SPM}$

31 was further applied to the Visible Infrared Imaging Radiometer Suite (VIIRS) measurements

32 over prominent coastal areas and produced reliable C_{SPM} maps along with realistic spatial

33 patterns. In contrast, applications of other C_{SPM} algorithms resulted in less reliable C_{SPM} maps

34 with either unjustified numerical discontinuities in the C_{SPM} spatial distribution or

35 unsatisfactory retrieval accuracy. Therefore, we propose GAA$_{SPM}$ as a preferred algorithm to

36 retrieve C_{SPM} over regions with a wide range of C_{SPM}, such as river plume areas.

37 **Keywords**: Remote Sensing Reflectance, Suspended Particulate Matter, Water Color, VIIRS,

38 Turbid Waters, Global Algorithm

39 1. Introduction

40   Suspended particulate matter (SPM) is one of the important water constituents that

41 determines water clarity. Knowledge of SPM dynamics in the estuarine and coastal waters

42 could advance our understanding of erosion and deposition processes, biomass primary

43 production, and the transport of sediments, nutrients, and heavy metals (Volpe et al., 2011).

44 Quantitative and accurate monitoring of the SPM dynamics has, therefore, long been desired

45 for effective coastal management and water quality assessment (Nechad et al., 2010).

46 Traditional methods with discrete sampling can only provide limited information on the

47 spatial-temporal variation of SPM. The remote sensing technique, on the other hand, can

48 provide frequent, synoptic, and consistent observations (IOCCG, 2000, 2006).

49   Because the concentration of SPM (C_{SPM}, in mg/L) can alter the appearance of water

50 color, there has been a long history of retrieving C_{SPM} from ocean color, such as the remote

51 sensing reflectance ($R_{rs}(\lambda)$, in sr^{-1}). Generally, $R_{rs}(\lambda)$ is a function of the total absorption and

52 backscattering coefficients ($a(\lambda)$ and $b_b(\lambda)$, respectively), and $a(\lambda)$ and $b_b(\lambda)$ are functions of

53 C_{SPM}. In extremely clear waters, particularly the ocean gyres, the extremely low

54 concentrations of suspended inorganic matter delivered from the air and the suspended

55 organic matter, such as phytoplankton detritus, do not contribute much to either $a(\lambda)$ or $b_b(\lambda)$,

56 resulting in a less sensitive correlation between $R_{rs}(\lambda)$ and C_{SPM}. The relatively large

57   uncertainties of the measured $R_{rs}(\lambda)$ and C_{SPM} in such waters could also contribute to the poor

58   $R_{rs}(\lambda)$-C_{SPM} correlation. With increasing C_{SPM}, $R_{rs}(\lambda)$ starts to be sensitive to C_{SPM}, especially

59   at visible bands (VIS) (Binding et al., 2005; Loisel et al., 2014). However, $R_{rs}(\lambda)$ in the visible

60   bands tend to saturate and the C_{SPM}-sensitive wavelength shifts to longer wavelength at the

61   near-infrared (NIR) bands in turbid waters (Luo et al., 2018; Shen et al., 2010a) and even to

62   the shortwave infrared (SWIR) bands in extremely turbid waters (Knaeps et al., 2015; Nechad

63   et al., 2010; Shi et al., 2018). As a result, C_{SPM} was preferably retrieved from $R_{rs}(\lambda)$ at the NIR

64   and SWIR bands for highly turbid waters (Doxaran et al., 2002a, 2002b, 2003; He et al., 2013;

65   Zhang et al., 2010).

66   However, existing algorithms were mostly developed for a specific range of C_{SPM} and are

67   not suitable for general applications in turbid estuarine and coastal waters, where C_{SPM} could

68   span over four orders of magnitude. Alternative methods were proposed with multiple

69   algorithms employed for different C_{SPM} ranges associated with hard-wired switching schemes

70   (Shen et al., 2010b; Shen et al., 2014). But using hard-wired switching schemes always come

71   with a demerit that the derived C_{SPM} will likely result in discontinuity, which is particularly

72   apparent when applying such schemes to satellite data (Shen et al., 2013). Switching

73   algorithms employing a blending scheme were also proposed to ensure a smooth transition

74   between algorithm output (Dogliotti et al., 2015; Han et al., 2016; Novoa et al., 2017).

75   However, these algorithms require reflectance values at certain wavelengths as the switching

76   boundaries, which differed significantly in the published studies. It is, thus, a challenge to

77   choose the 'right' boundaries for global applications. Therefore, novel and mechanistic

78   algorithms that can obtain smooth and natural coverage of C_{SPM} in coastal regions are still

79   strongly desired.

80   In this study, we propose a globally applicable algorithm for C_{SPM} retrieval (GAA$_{SPM}$) to

81   account for the shifting of the most sensitive $R_{rs}(\lambda)$ to increasing C_{SPM}. Calibration of GAA$_{SPM}$

82   was conducted by *in situ* data collected from multiple estuarine and coastal regions around the

83   world, resulting in reliable C_{SPM} retrievals for both clear and turbid waters. Further, GAA$_{SPM}$

84 was applied to the Visible Infrared Imaging Radiometer Suite (VIIRS) images and produced

85 reasonable C_{SPM} maps over turbid estuarine and coastal waters along with realistic spatial

86 patterns.

2. Data and Methods

2.1.   In situ datasets

89   Four *in situ* datasets with simultaneous measurements of C_{SPM} and $R_{rs}(\lambda)$ were employed

90 in this study for algorithm calibration and validation. The four datasets consist of the

91 Changjiang, the SeaSWIR, the University of Massachusetts Boston (UMB), and the Coastal

92 Surveillance through Observation of Ocean Color (COASTLOOC) datasets, with the

93 locations of sampling sites presented in Fig. 1.

2.1.1.   The Changjiang dataset

95   Three field campaigns were conducted in the Changjiang (Yangtze River, China) estuary

96 in February and June of 2011 and March of 2013. $R_{rs}(\lambda)$ spectra were measured by the

97 Hyperspectral Surface Acquisition System (HyperSAS, Satlantic Inc., Canada), which

98 concurrently measures the upwelling radiance above the sea surface ($L_t(\lambda)$, in W/m^2/nm/sr),

99 the sky radiance ($L_i(\lambda)$, in W/m^2/nm/sr), and the downwelling irradiance just above the

100 surface ($E_s(\lambda)$, in W/m^2/nm) from 350 to 858 nm in 136 spectral channels. The viewing

101 geometry of the mounted sensors was conformed to the NASA protocol to minimize sun glint

102 contamination (Fargion and Mueller, 2000). $R_{rs}(\lambda)$ was calculated from the radiometric

103 measurements following (Mobley, 1999),

$$R_{rs}(\lambda) = \frac{L_w(\lambda)}{E_s(\lambda)} = \frac{L_t(\lambda) - \rho L_i(\lambda)}{E_s(\lambda)} \tag{1}$$

104 where ρ is the sea-surface reflectance factor, which is a function of solar zenith angle and

105 surface roughness and is computed by the Ruddick-Hojerslev model (Ruddick et al., 2006).

106 The spectra of obtained $R_{rs}(\lambda)$ are presented in Fig. 2a.

107   Water samples were collected in duplicates concurrently with radiometric measurements

108 at each station and then filtered on board using pre-combusted (450°C for 6 h) and pre-

109   weighed GF/F glass microfiber filters (Whatman ®). Particle-loaded filters were rinsed three

110   times with Milli-Q water to remove dissolved salt and temporarily stored in a –20°C freezer

111   during the cruise. The filters were dried at 60°C for 24 h and then re-weighed in the

112   laboratory. SPM concentration of each sample was calculated as the difference between the

113   re-weighed particle-loaded filter and the pre-weighed blank filter and then divided by the

114   volume of filtered water. C_{SPM} of each station was averaged from the duplicate measurements,

115   which varied from 0.7 mg/L to 2068.8 mg/L with a mean value of 412.4 mg/L. Table 1

116   summarizes the four datasets with a brief description of each dataset.

117   *2.1.2 The SeaSWIR dataset*

118   The SeaSWIR dataset is a publicly available dataset, which consists of 137 concurrent

119   measurements of $R_{rs}(\lambda)$ and C_{SPM} at three turbid estuarine sites in the Gironde of France, the

120   Río de La Plata of Argentina, and the Scheldt of Belgium (Knaeps et al., 2018). $R_{rs}(\lambda)$ spectra

121   were measured by ASD (Analytical Spectral Devices, Inc.) with a spectral resolution of 1 nm

122   from 350 to 2500 nm. The SeaSWIR dataset provides only $R_{rs}(\lambda)$ from 350 to 1300 nm

123   because water is black beyond 1300 nm. Fig. 2b presents the $R_{rs}(\lambda)$ spectra of the SeaSWIR

124   data from 400 to 900 nm. SPM samples were also filtered using the GF/F filters with the

125   measured C_{SPM} ranging from 48.3 to 1400.5 mg/L and a mean value of 275.1 mg/L. Details

126   regarding the measurements of $R_{rs}(\lambda)$ and C_{SPM} are described in Knaeps et al. (2018).

127   *2.1.3 The UMB dataset*

128   The UMB dataset includes data collected from one cruise in the Gulf of Mexico in

129   September 2013 and four cruises in the Massachusetts Bay from June to November of 2018.

130    $R_{rs}(\lambda)$ spectra were measured by a floating system, named the Radiometer Incorporated

131   Skylight Blocked Apparatus (RISBA) (Lee et al., 2013). This RISBA is equipped with one

132   hyperspectral irradiance sensor and one radiance sensor (HyperOCI, Satlantic Inc.) with

133   radiometric measurements at ~ 3 nm increments from 350 to 800 nm. The radiance sensor,

134   incorporated with a custom designed cone, can measure spectral water-leaving radiance

135   ($L_w(\lambda)$) directly by blocking off the surface-reflected skylight. With simultaneously measured

136    $E_s(\lambda)$ by the irradiance sensor, $R_{rs}(\lambda)$ can be computed as the ratio of $L_w(\lambda)$ and $E_s(\lambda)$. The

137   computed $R_{rs}(\lambda)$ was later corrected for the instrument self-shadowing (Shang et al., 2017).

138   Note that RISBA was always kept > 20 m away from the ship to minimize ship perturbations

139   during the deployment. The uncertainties of measured $R_{rs}(\lambda)$ by RISBA are around 5% in

140   visible bands (Lee et al., 2013). The spectra of measured $R_{rs}(\lambda)$ are presented in Fig. 2c.

141   Determination of SPM concentration adopted the same method as described in Section 2.1.1,

142   with the measured C_{SPM} ranging from 0.2 to 30.6 mg/L and averaged at 5.7 mg/L.

143   *2.1.4 The COASTLOOC dataset*

144   The COASTLOOC dataset consists of 422 observations of marine reflectance and bio-

145   optical parameters collected from European coastal waters (Babin et al., 2003). It was the

146   irradiance reflectance just beneath the sea surface $R(\lambda, 0^-)$ available in the COASTLOOC

147   dataset instead of $R_{rs}(\lambda)$. The raw COASTLOOC dataset was filtered for concurrent

148   measurements of C_{SPM} and $R(\lambda, 0^-)$ at 411, 443, 456, 490, 509, 532, 619, 665, 683, 705, 779,

149   and 866 nm, where 99 observations were retained. SPM samples were also filtered using the

150   GF/F filters with the measured C_{SPM} ranging from 0.7 to 72.8 mg/L and averaged at 4.8 mg/L.

151   The $R(\lambda, 0^-)$ was converted to $R_{rs}(\lambda)$ based on Zhang and Fell (2007),

$$R_{rs}(\lambda) = \frac{1}{Q}\frac{t^2}{n^2}R(\lambda, 0^-) \tag{2}$$

152   where t is the transmittance of the air-sea interface, n is the real part of the complex refraction

153   index of seawater, and Q is the upwelling irradiance-to-radiance ratio. In this study, t^2/n^2 is

154   approximated by a constant factor of 0.54 (Austin, 1974) and Q is set to 4.0 (Loisel and Morel,

155   2001), resulting in $R_{rs}(\lambda) = 0.133\,R(\lambda, 0^-)$. Note that Q typically varies between 3.5 and 5.0

156   under typical measurement conditions (Loisel and Morel, 2001). A simplified solution to Eq.

157   (2) with constant Q will introduce uncertainties to calculated $R_{rs}(\lambda)$. However, the

158   dependencies of Q could be mostly canceled out when $R_{rs}(\lambda)$ ratios are used for algorithm

159   development (Zhang and Fell, 2007).

160   Since $R_{rs}(745)$ is required in this study for algorithm development, while this wavelength

161   is absent from the COASTLOOC dataset, the multispectral $R_{rs}(\lambda)$ was interpolated to

162   hyperspectral $R_{rs}(\lambda)$ using a semi-analytic approach (described in Appendix 1). The spectral

163    $R_{rs}(\lambda)$ of the retained COASTLOOC observations are shown in Fig. 2d. Note that

164   uncertainties of the interpolated $R_{rs}(745)$ could have minimal impacts on the derived C_{SPM} for

165   the COASTLOOC dataset as C_{SPM} is generally low in this dataset (see discussions in Section

166   4.2).

167   *2.2.   VIIRS and atmospheric correction*

168   VIIRS, onboard the Suomi National Polar-orbiting Partnership (SNPP) satellite, is one of

169   the operational moderate resolution ocean color imagers with a spatial resolution of 750 m.

170   VIIRS-SNPP acquires radiometric measurements at seven spectral bands from the visible to

171   NIR, with the nominal center wavelengths of 410, 443, 486, 551, 671, 745, and 862 nm. In

172   this study, VIIRS images were atmospherically corrected by the NOAA Multi-Sensor Level-1

173   to Level-2 (MSL12) ocean color data processing system using a combined NIR and SWIR

174   atmospheric correction algorithm (Wang, 2007; Wang and Shi, 2007). The NIR-SWIR

175   algorithm proceeds with the standard NIR algorithm for the open oceans (Gordon and Wang,

176   1994), whereas the SWIR algorithm is used for the turbid waters in coastal regions (Wang,

177   2007; Wang and Shi, 2007). The NIR algorithm assumes 'black ocean' at the NIR bands (745

178   and 862 nm), while the SWIR algorithm adjusts the assumption to the SWIR bands (1238 and

179   1601 nm) for turbid waters (Jiang and Wang, 2014). A turbid water index, developed by Shi

180   and Wang (2007), is pre-computed to identify the turbid water pixels where the SWIR

181   algorithm can be implemented.

182   To evaluate the performance of VIIRS $R_{rs}(\lambda)$ products, satellite match-up pairs were

183   acquired over a 3-by-3-pixel window centered at the *in situ* sampling site with the following

7

184 criteria applied. First, the field-measured $R_{rs}(\lambda)$ were sampled within one hour of the VIIRS-

185 SNPP overpass. The selected time difference is to account for the significant spatial-temporal

186 variabilities of water masses in estuarine and coastal waters due to the strong tide and rapid

187 current and runoff. Second, at least 50% of the pixels were valid within the 3-by-3-pixel

188 window. All pixels flagged as land, cloud, cloud straylight or shadow contamination, high

189 glint, and atmospheric correction failure were considered invalid. For the SeaSWIR dataset,

190 this threshold was relaxed to 30% because some of the sampling sites were dock-based, and at

191 least one-third of the 3-by-3-pixel window is flagged as land. At last, the median $R_{rs}(\lambda)$ of the

192 3-by-3-pixel window was used as satellite-derived $R_{rs}(\lambda)$.

193 *2.3.   Algorithms for C_{SPM} retrievals*

194 The Changjiang and UMB datasets do not have $R_{rs}(862)$ that required for algorithm

195 development. For the Changjiang dataset, which has comparable C_{SPM} range with the

196 SeaSWIR dataset (Table 1), $R_{rs}(862)$ is computed from measured $R_{rs}(858)$ using the $R_{rs}(862)$-

197 $R_{rs}(858)$ relationship calibrated from the SeaSWIR dataset ($R^2 = 1$, N = 137),

$$R_{rs}(862) = 0.983 \times R_{rs}(858). \tag{3}$$

198 For the UMB dataset, which has similar C_{SPM} range as the COASTLOOC dataset (Table

199 1), $R_{rs}(862)$ is computed from measured $R_{rs}(800)$ using a calibrated relationship between

200 interpolated $R_{rs}(800)$ and $R_{rs}(862)$ from the COASTLOOC dataset ($R^2 = 0.96$, N = 98),

$$R_{rs}(862) = 0.483 \times R_{rs}(800). \tag{4}$$

201 The empirical relationship of Eq. (4) could introduce extra errors to the calculated

202 $R_{rs}(862)$. However, these errors should have minimal impacts on the derived C_{SPM} for the

203 UMB dataset due to the low C_{SPM} values, as discussed in Section 4.2.

204 *2.3.1.   Development of a novel algorithm for wide-range C_{SPM}*

205 C_{SPM} and $R_{rs}(\lambda)$ data pairs were partitioned into four subsets to evaluate the sensitivity of

206 $R_{rs}(\lambda)$ to separate C_{SPM} ranges. The four groups are defined by the C_{SPM} range and are

207 classified as 'clear' waters ($C_{SPM} < 1$ mg/L, N = 47), 'low turbidity' waters ($1 < C_{SPM} < 10$

208   mg/L, N = 132), 'moderate turbidity' waters ($10 < C_{SPM} < 50$ mg/L, N = 41), and 'high

209   turbidity' waters ($C_{SPM} > 50$ mg/L, N =217), respectively. Note that the selection of such

210   criteria is somewhat arbitrary but can adequately demonstrate the sensitivity of $R_{rs}(\lambda)$ to

211   increasing C_{SPM}.

212   The coefficient of determination (R^2) from linear regressions between C_{SPM} and $R_{rs}(\lambda)$ at a

213   single VIIRS band and the band ratio of $R_{rs}(\lambda)$ over $R_{rs}(551)$ for the four subsets are shown in

214   Fig. 3. As presented in Fig. 3a, the most sensitive $R_{rs}(\lambda)$ to C_{SPM} shifts progressively from

215   671 nm to 862 nm with increasing C_{SPM}, which is consistent with the results in Shen et al.

216   (2010b). It is worthy to note that the ratios of $R_{rs}(\lambda)$ to $R_{rs}(551)$ have higher R^2 values with

217   C_{SPM} than the individual $R_{rs}(\lambda)$. Therefore, C_{SPM} could be more sensitive to the band ratios,

218   which is likely due to the fact that using band ratios can partially remove the effects of bi-

219   directional variations of $R_{rs}(\lambda)$ (Doxaran et al., 2006). Therefore, $R_{rs}(\lambda)$ to $R_{rs}(551)$ ratios,

220   rather than $R_{rs}(\lambda)$ values, are employed in this study to develop the retrieval algorithm for

221   C_{SPM}.

222   Given that the sensitive wavelength in $R_{rs}(\lambda)$ for C_{SPM} varies with increasing C_{SPM}, band

223   ratios of $R_{rs}(671)$, $R_{rs}(745)$, and $R_{rs}(862)$ over $R_{rs}(551)$ are all included to retrieve C_{SPM} for

224   waters from ocean to turbid river mouths. More importantly, we introduce weighting factors

225   to progressively adjust the weights of the three band ratios to effectively account for the shift

226   of the $R_{rs}(\lambda)$ to the C_{SPM}-sensitive wavelength. As a result, a generalized index for SPM (GI_{SPM})

227   is formulated,

$$GI_{SPM} = c_0 \times \frac{R_{rs}(551)}{R_{rs}(486)} + \sum_{i=1}^{3} c_i \times W_i \times \frac{R_{rs}(\lambda_i)}{R_{rs}(551)} \qquad (5)$$

228   where c_{0-3} are empirical coefficients, and W_{1-3} are the weighting factors for $R_{rs}(\lambda)$ at λ_1 (671

229   nm), λ_2 (745 nm), and λ_3 (862 nm), respectively. W_i is defined as,

$$W_i = \frac{R_{rs}(\lambda_i)}{R_{rs}(\lambda_1) + R_{rs}(\lambda_2) + R_{rs}(\lambda_3)}, \quad i = 1, 2, 3 \qquad (6)$$

230   The band ratio $R_{rs}(551)/R_{rs}(486)$ in Eq. (5) is introduced to partially and empirically

231   account for the variation of chlorophyll-a concentration in clear and low turbidity waters, as it

232   may also contribute to the ratio of $R_{rs}(671)/R_{rs}(551)$. The SPM concentration is finally

233   calculated from the GI_{SPM} using a power-law function,

$$C_{\text{SPM}} = a_1 \times [GI_{SPM}]^{a_2} \tag{7}$$

234   where a_1 and a_2 are the algorithm coefficients. Values of the algorithm constants (c_{0-3} and a_{1-2})

235   in Eq. (5) and Eq. (7) were calculated from nonlinear least-square-fit using paired C_{SPM} and

236    $R_{rs}(\lambda)$ ratios from the *in situ* datasets, with results as 20.43, 2.15, 0.04, 1.17, 0.4, and 14.86 for

237   a_1, a_2, c_0, c_1, c_2, and c_3, respectively (also see Table 2). Note that it is dimensionless for the

238   coefficients c_{0-3} and a_2, while the units for a_1 is mg/L.

239   *2.3.2.   Other retrieval algorithms for C_{SPM}*

240   Table 3 lists a few typical algorithms in the literature that are employed in this study for

241   algorithm inter-comparison. The second column in Table 3 presents the algorithm formulae

242   and coefficients as in the literature, while the third column shows adjusted algorithm

243   coefficients that are recalibrated using the *in situ* datasets of this effort. The Dsa_07 (D'Sa et

244   al., 2007) was explicitly proposed for relatively clear waters and was recalibrated using data

245   with $C_{\text{SPM}} < 50$ mg/L only. The Doxaran_02 (Doxaran et al., 2002a) and He_13 (He et al.,

246   2013) were perceived appropriate for turbid waters only, and they were therefore recalibrated

247   using data with $C_{\text{SPM}} > 50$ mg/L. The Geostationary Ocean Color Imager (GOCI) algorithm in

248   Table 3 is the standard C_{SPM} algorithm for processing GOCI data, which employs two

249   respective algorithms for less-turbid and turbid waters (Min et al., 2013; Siswanto et al.,

250   2011). In this study, GOCI and Shen_10 (Shen et al., 2010b) used the same hard-wired

251   switching scheme to estimate C_{SPM} for less turbid waters ($C_{\text{SPM}} < 50$ mg/L) and highly turbid

252   waters ($C_{\text{SPM}} > 50$ mg/L), with a switching threshold of $R_{rs}(671) = 0.02$ sr^{-1}. We followed this

253   approach for consistency, also because 97% of highly turbid samples in our datasets having

254    $R_{rs}(671) > 0.02$ sr^{-1} and 94% of the less-turbid samples having $R_{rs}(671) < 0.02$ sr^{-1}.

255   In addition to the relatively simple empirical algorithms described in Table 3, we also

256   included Mao_12 (Mao et al., 2012), Dogliotti_15 (Dogliotti et al., 2015), Han_16 (Han et al.,

257   2016), Novoa_17 (Novoa et al., 2017), and Gohin_05 (Gohin et al., 2005) for algorithm inter-

258   comparison. The first four algorithms were proposed to retrieve wide-range C_{SPM} with a

259   smooth transition from relatively clear to highly turbid waters, while Gohin_05 was for

260   relatively clear waters only.

261   *2.3.2.1 The Mao_12 algorithm*

262   The Mao_12 algorithm uses a rather complicated system with four indices to formulate a

263   proxy (P) for C_{SPM}. Steps to illustrate the Mao_12 algorithm are summarized below,

$$X1 = (R_{rs}(\lambda))/(\eta - R_{rs}(\lambda)) \tag{8}$$

$$X2 = (R_{rs}(\lambda_1))/(R_{rs}(\lambda_2)) \tag{9}$$

$$X3 = \sum R_{rs}(\lambda_i) \tag{10}$$

$$X4 = \sum \delta R_{rs}(\lambda_i)/\delta\lambda_i \tag{11}$$

$$P = (f_1 X1 + f_2 X2 + f_3 X3 + f_4 X4)/\sum_{i=1}^{4} f_i \tag{12}$$

$$C_{\text{SPM}} = 10^{(b_1 + b_2 * P)} \tag{13}$$

264   where $X1$, $X2$, $X3$, and $X4$ are the four indices, and the wavelengths in each index are selected

265   based on the highest correlation coefficients of the regression analysis between the index and

266   C_{SPM}. η in Eq. (8) is determined along with the selected wavelength for $X1$. $X4$ is the sum of

267   the spectral slope at each wavelength, which is calculated from the derivation of two

268   neighboring $R_{rs}(\lambda)$ in relation to their wavelengths.

269   The Mao_12 algorithm was initially calibrated at the center bands of Sea-viewing Wide

270   Field-of-view Sensor (SeaWiFS), which are 412, 443, 490, 510, 555, 670, 765, and 865 nm,

271   respectively. Specifically, $X1$ is computed at 670 nm with η as 0.085. $X2$ is the band ratio of

272    $R_{rs}(765)$ to $R_{rs}(510)$. $X3$ is the sum of $R_{rs}(\lambda)$ at 510 and 765 nm. $X4$ is the sum of spectral

273   slopes at all SeaWiFS bands except 412 and 865 nm. The original values of f_{1-4} and b_{1-2} are

274   0.3, 0.2, 10, 1, 0.947, and 0.775, respectively. These empirical coefficients are re-tuned using

275   our datasets with wavelengths for each index selected from the VIIRS center bands. As a

276   result, $X1$ is computed from $R_{rs}(862)$ with η now as 0.075. $X2$ is the band ratio of $R_{rs}(862)$ to

277     $R_{rs}(551)$. $X3$ is the sum of $R_{rs}(\lambda)$ at 671, 745, and 862 nm. $X4$ is the sum of spectral slopes at

278   all VIIRS-SNPP bands except for 410 and 862 nm. The recalibrated values of $f_{1\text{-}4}$ and $b_{1\text{-}2}$ are

279   –0.49, 1.22, 9.37, 0.37, 14.29, and –0.08, respectively.

280   *2.3.2.2 The Dogliotti_15 algorithm*

281   Nechad et al. (2010) proposed a generic algorithm to directly retrieve C_{SPM} from a single

282   band water-leaving reflectance ($\rho_w(\lambda) = \pi\, R_{rs}(\lambda)$, dimensionless). Dogliotti et al. (2015)

283   adapted the Nechad et al. (2010) algorithm and used two respective algorithms to retrieve

284   C_{SPM} for relatively clear and turbid waters,

$$C_{\text{SPM\_clear}} = A_T(\lambda_1)\rho_w(\lambda_1)/(1 - \rho_w(\lambda_1)/C(\lambda_1)) \tag{14}$$

$$C_{\text{SPM\_tur}} = A_T(\lambda_2)\rho_w(\lambda_2)/(1 - \rho_w(\lambda_2)/C(\lambda_2)) \tag{15}$$

285   where $A_T(\lambda)$ and $C(\lambda)$ are wavelength-dependent calibration coefficients and λ_1 and λ_2 are set

286   to 645 and 859 nm, respectively. The originally values of $A_T(\lambda)$ and $C(\lambda)$ were 228.1 and

287   0.164 for λ_1, and 3078.9 and 0.211 for λ_2, respectively. A switching scheme was also

288   proposed where $C_{\text{SPM}} = C_{\text{SPM\_clear}}$ when $\rho_w(645) < 0.05$ and $C_{\text{SPM}} = C_{\text{SPM\_tur}}$ when $\rho_w(645) >$

289   0.07. For $\rho_w(645)$ between 0.05 and 0.07, $C_{\text{SPM}} = (1\text{-}w)\, C_{\text{SPM\_clear}} + w\, C_{\text{SPM\_tur}}$, with w as the

290   weighting factor changed linearly from 0 at $\rho_w(645) = 0.05$ to 1 at $\rho_w(645) = 0.07$.

291   In this study, we recalibrated the Dogliotti_15 algorithm for VIIRS bands (*i.e.* $\lambda_1 = 671$

292   nm and $\lambda_2 = 862$ nm) using the four *in situ* datasets, with recalibrated $A_T(\lambda)$ and $C(\lambda)$ as 227.5

293   and 0.1736 for λ_1, and 2485.1 and 0.2155 for λ_2, respectively. The same switching and

294   blending schemes were adopted here but using $\rho_w(671)$ values as the switching boundaries.

295   *2.3.2.3 the Han_16 algorithm*

296   Han et al. (2016) also developed two algorithms for clear and turbid waters based on the

297   algorithm of Nechad et al. (2010). The same Eqs. (14) and (15) are employed for Han_16, but

298   with λ_1 and λ_2 set to 671 and 745 nm, respectively. Note that Han_16 also provides an option

299   of using $\rho_w(671)$ to estimate C_{SPM} for turbid waters, which is not considered in this study due

300   to the saturation of $\rho_w(671)$ over extremely turbid waters (Shi and Wang, 2014). The original

301    $A_T(\lambda)$ and $C(\lambda)$ in Han et al. (2016) were set to 389.5 and 0.5 for 671 nm, and 2220.1 and 0.4

302   for 745 nm, respectively. In this study, $A_T(\lambda)$ and $C(\lambda)$ were recalibrated using our datasets,

303   and the optimized values are 227.2 and 0.35 for 671 nm, and 2338.8 and 0.23 for 745 nm,

304   respectively. Han et al. (2016) proposed a different blending scheme from Dogliotti_15,

305   which is expressed as,

$$C_{SPM} = \frac{W_c * C_{SPM\_clear} + W_t * C_{SPM\_tur}}{W_c + W_t} \qquad (16)$$

306   where W_c and W_t are the weights for the estimated C_{SPM} for clear and turbid waters,

307   respectively, and are calculated from $R_{rs}(671)$. Specifically, for $R_{rs}(671) < 0.03$ sr^{-1}, W_c is set

308   to 1 and W_t is set to 0. For $R_{rs}(671) > 0.04$ sr^{-1}, W_c is set to 0 and W_t is set to 1. For $R_{rs}(671)$

309   between the two boundaries, W_c and W_t are defined as,

$$W_c = log10(0.04) - log10[R_{rs}(671)] \qquad (17)$$

$$W_t = log10[R_{rs}(671)] - log10(0.03) \qquad (18)$$

310   *2.3.2.4 the Novoa_17 algorithm*

311   Novoa et al. (2017) proposed a multi-conditional algorithm for C_{SPM} retrieval, which

312   switches among five different algorithms based on the $\rho_w(671)$ values. The Novoa_17

313   algorithm is described in Table 4. The 'Original' expressions in Table 4 employ the calibrated

314   coefficients from Novoa et al. (2017), while the 'Recalibrated' expressions use coefficients

315   recalibrated from the *in situ* datasets of this study. Novoa_17 has three key algorithms

316   (C_{SPM_Green}, C_{SPM_Red}, and C_{SPM_Green} in Table 4) for clear, moderately turbid, and highly turbid

317   waters, respectively, and uses two blending algorithms ($C_{SPM\_Green-Red}$ and $C_{SPM\_Red-NIR}$) to

318   obtain smooth transitions of the estimated C_{SPM}. The weighting factors (α_{1-2} and β_{1-2}) for

319    $C_{SPM\_Green-Red}$ and $C_{SPM\_Red-NIR}$ in Table 4 are calculated as following,

$$\alpha_1 = \ln\left(\frac{S_{L95+}}{\rho_w(671)}\right) / \ln\left(\frac{S_{L95+}}{S_{L95-}}\right), \beta_1 = \ln\left(\frac{\rho_w(671)}{S_{L95-}}\right) / \ln\left(\frac{S_{L95+}}{S_{L95-}}\right) \qquad (19)$$

$$\alpha_2 = \ln\left(\frac{S_{H95+}}{\rho_w(671)}\right) / \ln\left(\frac{S_{H95+}}{S_{H95-}}\right), \beta_2 = \ln\left(\frac{\rho_w(671)}{S_{H95-}}\right) / \ln\left(\frac{S_{H95+}}{S_{H95-}}\right) \qquad (20)$$

where S_{L95+} and S_{L95-} are the lower smoothing bounds derived from the 95% confidence levels

of the regression curve between $\rho_w(671)$ and $\rho_w(551)$, while S_{H95+} and S_{H95-} are the higher

smoothing bounds derived from the $\rho_w(862)$-$\rho_w(671)$ regression curve (See Figure 4 in Novoa

et al. (2017) for details). S_{L95+}, S_{L95-}, S_{H95+}, and S_{H95-} are provided in Novoa et al. (2017) with

values of 0.007, 0.016, 0.08, and 0.2, respectively, for Gironde estuary measurements. We

adopted these values to evaluate the validity of Novoa_17 in this study.

2.3.2.5 Gohin_05 algorithm

Gohin et al. (2005) assumed that C_{SPM} could be estimated as the sum of the concentrations

by non-living SPM (SPM_{nLv}) and organic SPM (SPM_o). Specifically, SPM_{nLv} can be derived

from normalized water-leaving reflectance at the green or red bands with assumptions of

constant mass-specific particulate absorption and backscattering coefficients (See their Eq.

(18) and Table 3 for details). The SPM_o can be converted from the concentration of

particulate organic carbon (POC), which can be estimated from chlorophyll-a concentration

([Chl]). As a result, the Gohin_05 algorithm can be expressed as,

$$C_{SPM} = SPM_{nLv} + 234[Chl]^{0.57}, \qquad (21)$$

where [Chl] is retrieved from a five-band algorithm using a specific look-up-table (LUT)

(Gohin et al., 2002). Note that the recalibration of Gohin_05 was not performed in this study,

given that only a few [Chl] measurements in our datasets can be found to update the LUT.

Therefore, in this study, we evaluate the performance of Gohin_05 using its original LUT and

mass-specific particulate absorption and backscattering coefficients, provided by Dr. Francis

Gohin at the authors' request.

2.4. Statistical measures for model performance

To evaluate the performance of each algorithm, several statistical measures were

introduced in this study, including the slope, the coefficient of determination (R^2), the relative

mean absolute difference (rMAD), and the root mean square difference (RMSD). The slope

and R^2 are computed from the linear regression between the measured and the derived C_{SPM}

using the Model-II regression (Laws, 1997). The rMAD and RMSD are defined by,

$$\text{rMAD} = \sum |1 - \text{derived/measured}|/\text{N} \times 100\% \qquad (18)$$

$$\text{RMSD} = \sqrt{\sum (\text{derived} - \text{measured})^2 /\text{N}} \qquad (19)$$

346 where N is the number of data points.

347 The performances of the abovementioned algorithms from the literature were first

348 evaluated by applying them to the four *in situ* datasets using their original algorithm

349 coefficients. Statistic measures are tabulated in Table 5, where the derived C_{SPM} from these

350 algorithms are found with relatively large uncertainties, except for the Doxaran_02. Such

351 performances are likely due to both data characteristics and data processing, as empirical

352 algorithms are always data dependent. Therefore, a re-tuning of the algorithm coefficients is

353 necessary to ensure apple-to-apple comparisons between these algorithms and GAA$_{SPM}$.

354 For the recalibrated algorithms, model win rate (MWR) (Seegers et al., 2018) is adopted

355 here as an additional metric to evaluate the algorithm performance. A pair-wise comparison of

356 the absolute residual difference (= |derived – measured|) was performed for each sample, and

357 the algorithm with a lower residual was designated as the winner. MWR is defined as the

358 percent wins for each algorithm. In this study, each algorithm was pair-to-pair compared to

359 other candidate algorithms to calculate the MWR. We adopted the average MWR of each

360 algorithm as the metric to evaluate its overall performance, which is hereafter referred to as

361 the overall win rate (OWR).

362 **3. Results**

363 *3.1. Inter-comparison of C_{SPM} retrieval algorithms*

364 Validation results of GAA$_{SPM}$, as well as these recalibrated algorithms described in

365 Section 2.3, are presented in Fig. 4. Considering the applicable range of each C_{SPM} algorithm,

366 the performance of each algorithm was evaluated for the entire C_{SPM} range, the subset of less

367 turbid waters (C_{SPM} < 50 mg/L), and the subset of highly turbid waters (C_{SPM} > 50 mg/L),

368 respectively. Statistic measures of each algorithm for the three C_{SPM} range are given in Table

369 6.

370   Evaluation of algorithms over the entire C_{SPM} range shows that GAA$_{SPM}$ has the best

371 performance with points more closely distributed to the 1:1 line (Fig. 4a). GAA$_{SPM}$ also has

372 the highest R^2 (0.91), and the smallest rMAD (41.3%) and RMSD (122.0 mg/L) for the

373 derived C_{SPM} among all algorithms that have valid retrievals over the entire C_{SPM} range (Table

374 6). Dogliotti_15 and Shen_10 also have comparable C_{SPM} retrieval accuracy with GAA$_{SPM}$

375 with rMADs of 44.6% and 42.5%, respectively, followed by the GOCI with an rMAD of

376 46.3%. The OWRs of GAA$_{SPM}$, Dogliotti_15, and Shen_10 over the entire C_{SPM} range also

377 confirm their comparable performance, with the values of 57.9%, 58.0, and 56.8%,

378 respectively. Note that the performance of GAA$_{SPM}$, Dogliotti_15, GOCI, and Shen_10 in

379 highly turbid waters are very consistent (rMAD ~ 32%). Therefore, the better performance of

380 GAA$_{SPM}$ over the entire C_{SPM} range is because GAA$_{SPM}$ also performs well in less turbid

381 waters (Table 6).

382   In addition, including OWR as one of the metrics allows for a better understanding of the

383 error distribution for each algorithm. For example, the performance of Shen_10 and GAA$_{SPM}$

384 in highly turbid waters are very comparable in terms of rMAD (32.6% and 32.2%,

385 respectively), but OWR of Shen_10 (= 64.7%) is much higher than that of GAA$_{SPM}$ (= 54.4%),

386 suggesting that more retrievals from Shen_10 are with large residuals, or 'outliers'. Detailed

387 discussion on these different metrics and their advantages and disadvantages can be referred

388 to Seegers et al. (2018).

389   Other algorithms capable of wide-range C_{SPM} retrieval, Novoa_17, Han_16, and Mao_12,

390 are found with relatively larger uncertainties in terms of both rMAD and RMSD. Mao_12 is

391 observed with significant uncertainties for highly turbid waters with an rMAD of 61.7%,

392 which is mainly attributed to the significantly underestimated C_{SPM} within the 50 – 400 mg/L

393 range (see Fig. 4e). The relatively larger uncertainties of Novoa_17 and Han_16 are also

394 attributed to the retrievals in moderately turbid waters, especially for those of the SeaSWIR

16

395   dataset (see Fig. 4b and Fig. 4d). In addition, Han_16 uses $R_{rs}(745)$ instead of $R_{rs}(862)$ for

396   C_{SPM} retrieval in extremely turbid waters, which results in saturated retrievals of C_{SPM}.

397   Dsa_07 and Gohin_05 were explicitly developed for less turbid waters. However,

398   evaluations of Dsa_07 and Gohin_05 show that they have relatively larger uncertainties

399   compared with GAA$_{SPM}$. For Dsa_07, it appears that the algorithm is no longer sensitive for

400   C_{SPM} below 5 mg/L (Fig. 4h). For Gohin_05, as it has not been recalibrated or optimized

401   using our datasets, the relatively larger uncertainties could be expected (Fig. 4i).

402   Evaluation results of Doxaran_02 and He_13, explicitly proposed for highly turbid waters,

403   are presented in Fig. 4j and Fig. 4k, respectively. Doxaran_02 has been observed with the

404   smallest rMAD of 31.6%, followed by GAA$_{SPM}$ with an rMAD of 32.2%. He_13, on the other

405   hand, has relatively larger uncertainties with an rMAD of 42.5%, which is likely because that

406   He_13 utilizes $R_{rs}(745)$ instead of $R_{rs}(862)$ for C_{SPM} retrieval, as $R_{rs}(862)$ is more sensitive to

407   C_{SPM} of highly turbid waters. However, it appears that GAA$_{SPM}$ could arguably perform the

408   best for the turbid subset as GAA$_{SPM}$-retrieved C_{SPM} has the highest R^2 (0.88) and smallest

409   RMSD (174.23 mg/L) among all algorithms (Table 6). Further discussions of GAA$_{SPM}$ are

410   presented in Section 4.1.

411   *3.2.   SPM mapping products*

412   The NIR-SWIR atmospheric correction algorithm was first evaluated by comparing

413   satellite-derived $R_{rs}(\lambda)$ with match-up $R_{rs}(\lambda)$ from ground measurements, which is presented

414   in Fig. 5. Overall, good agreements are observed between the field-measured $R_{rs}(\lambda)$ and the

415   VIIRS-derived $R_{rs}(\lambda)$ at 486, 551, and 671 nm, with rMADs of 18.7%, 14.3%, and 15.4%,

416   respectively. However, significant uncertainties are observed for VIIRS-derived $R_{rs}(\lambda)$ at 443,

417   745, and 862 nm, with rMADs of 38.2%, 108.1%, and 79.4%, respectively. Since the band

418   443 nm is not involved in GAA$_{SPM}$, the uncertainties of VIIRS $R_{rs}(443)$ will not be discussed

419   in this study. The large uncertainties of $R_{rs}(745)$ and $R_{rs}(862)$ are mainly observed in

420   relatively clear waters, but their impacts on the derived C_{SPM} by GAA$_{SPM}$ can be neglected in

421 such waters (see discussions in Section 4.2). Note that validation of the NIR-SWIR

422 atmospheric correction algorithm was not performed for extremely turbid waters due to no

423 available match-ups in this study. However, previous efforts have demonstrated that the NIR-

424 SWIR algorithm could yield accurate R_{rs}(NIR) over turbid coastal and estuarine waters for

425 multiple satellite data, including the VIIRS-SNPP (Wang et al., 2011; Wang et al., 2007).

426 Therefore, the NIR-SWIR atmospheric correction is deemed to be adequate for C_{SPM} retrieval

427 in both clear and turbid waters.

428   In this study, as demonstrations, GAA$_{SPM}$ was applied to VIIRS-SNPP $R_{rs}(\lambda)$ products to

429 map the spatial distribution of C_{SPM} over two highly turbid estuaries: China's Changjiang

430 estuary and Argentina's Río de La Plata estuary. The recalibrated Novoa_17, Dogliotti_15,

431 Shen_10, GOCI, and Mao_12 algorithms were also implemented to the same VIIRS-SNPP

432 data for algorithm inter-comparison.

433   The six C_{SPM} retrieval algorithms were first implemented to a VIIRS-SNPP image

434 acquired on April 8, 2018, over the Changjiang estuary with the C_{SPM} mapping products

435 presented in Figs. 6a - 6f. Overall, the C_{SPM} mapping products by the six algorithms present

436 similar patterns in the spatial distribution where high C_{SPM} is frequently found in the Subei

437 Coast and the Hangzhou Bay (see their respective locations in Fig. 6a). A decreasing trend of

438 C_{SPM} can be observed from the coast to the offshore waters, and rapid declines of C_{SPM} occur

439 at the front of the turbidity plume. The major differences among these mapping products lie in

440 the range of the derived C_{SPM}, especially for C_{SPM} in the offshore areas and the turbidity

441 maxima zone.

442   It is difficult to quantitatively evaluate the accuracy of the C_{SPM} maps due to the lack of

443 high-quality satellite-ground match-ups. Notably, the spatial variation of the "ground-truth"

444 C_{SPM} at the VIIRS pixel scale (750 m $\times$ 750 m) cannot be neglected for turbid estuaries. As a

445 result, discrepancies between VIIRS-derived and *in situ*-measured C_{SPM} could be expected

446 even for a "perfect" match-up on time and location, not to mention that VIIRS $R_{rs}(\lambda)$ is

447 derived from a 3-by-3-pixel window. However, the ranges of the derived C_{SPM} by the six

448 algorithms could give some insights into their respective performances. For the offshore

449 waters, the derived C_{SPM} by GAA_{SPM}, Dogliotti_15, Mao_12, and GOCI are overall

450 comparable, while Shen_10 produces much lower C_{SPM}, and Novoa_17 yields relatively

451 higher C_{SPM}. As an indirect validation, the measured C_{SPM} at the offshore area, highlighted in

452 Fig. 6b with the red dashed rectangle, in March of 2013 was between 0.7 and 6.8 mg/L with

453 an average C_{SPM} of 3.4 mg/L (N =14), which agrees well with the retrievals by GAA_{SPM},

454 Dogliotti_15, and GOCI (Figs. 6a, 6c, and 6e).

455   Variations of the retrieved C_{SPM} along a transect (Lines A Fig. 6a) also confirm the

456 consistent estimations of C_{SPM} by GAA_{SPM}, Dogliotti_15, and GOCI in offshore waters (see

457 Fig. 6h and Fig. 6i). Compared with GAA_{SPM}, Mao_12 seems to underestimate the C_{SPM} for

458 low and moderate turbidity waters (see Fig. 6h), which is also observed in Fig. 4e. For the

459 turbidity maxima zones in the Hangzhou Bay and the Subei Coast, the derived C_{SPM} ranges by

460 the GAA_{SPM} and Shen_10 are overall comparable, while GOCI predicts slightly lower C_{SPM}

461 and Mao_12 yields much higher C_{SPM}. Compared with GAA_{SPM}, Novoa_17 seems to

462 overestimate C_{SPM} in moderate turbidity waters, such as in the Southern part of the Subei

463 Coast. Dogliotti_15, on the other hand, could probably underestimate C_{SPM} in the turbidity

464 maxima zone in the Hangzhou Bay. As mentioned in Dogliotti et al. (2015), the Dogliotti_15

465 algorithm tends to saturate in high turbidity waters, which could result in the underestimations

466 of C_{SPM}. As shown in Fig. 4c, we do observe the tendency of underestimation of

467 Dogliotti_15-derived C_{SPM} for $C_{SPM} > 1,000$ mg/L. Note that measured C_{SPM} from the turbid

468 zones in the Hangzhou Bay reached 2,000 mg/L in February, which is close to the predicted

469 results by GAA_{SPM} and Shen_10. Therefore, we could argue that VIIRS-derived C_{SPM} by the

470 GAA_{SPM} and Shen_10 in turbid waters could be more reasonable. However, further evaluation

471 with rigorously matched ground measurements is still required, since C_{SPM} in the Changjiang

472 estuary frequently changes in both magnitude and the spatial distribution.

473   In addition, discontinuities of the derived C_{SPM} are observed at the front of the turbidity

474 plume by Shen_10 and GOCI, as shown in Fig. 6e and Fig. 6f, which are attributed to the

475 same hard-wired switching scheme employed by these two algorithms. For areas straddling

476   the threshold pixel with $R_{rs}(670) = 0.02$ sr^{-1}, two different algorithms were applied to derive

477   C_{SPM}, which causes a sudden change of the derived C_{SPM} for the neighboring pixels. The

478   numerical discontinuities of VIIRS-derived C_{SPM} by Shen_10 and GOCI are better visualized

479   by the variations of the derived C_{SPM} along the one transect from the coast to the outer shelf

480   (Line A in Fig. 6a). Transect A spans over both clear and highly turbid waters and, therefore,

481   allows synoptic views of the performance of the six algorithms in different types of waters.

482   As highlighted by the dashed ellipse in Fig. 6g, sudden declines of VIIRS-derived C_{SPM} by

483   Shen_10 and GOCI are observed around the threshold pixel, with the derived C_{SPM} varies by

484   1 - 2 orders of magnitude for the two neighboring pixels. Although there might exist real

485   discontinuities of C_{SPM} in natural waters, such discontinuities should also be reflected in R_{rs}

486   measurements. However, $R_{rs}(671)$ along the transect A shows rapid decreases at the front of

487   the turbidity plume but no sudden and significant drop in values (see Fig. 6h). Therefore, the

488   discontinuities observed in the C_{SPM} mapping products of Shen_10 and GOCI are directly

489   introduced by the hard-wired switching schemes. The proposed GAA$_{SPM}$, on the other hand,

490   uses a progressive index and could avoid the numerical discontinuity. The Novoa_17,

491   Dogliotti_15, and Mao_12 algorithms can provide continuous C_{SPM} maps as well, but their

492   overall performance is less robust as GAA$_{SPM}$.

493   The six algorithms were also employed to map C_{SPM} over another turbid estuary, the Río

494   de La Plata estuary of Argentina, and the C_{SPM} mapping products are presented in Fig. 7.

495   Consistent with the results from the Changjiang estuary shown in Fig. 5, GAA$_{SPM}$ has

496   comparable C_{SPM} retrievals with Shen_10 in relatively turbid waters from the river mouth to

497   the front of turbidity plume, while the derived C_{SPM} by Novoa_17, Dogliotti_15, and GOCI

498   are slightly lower in such an area. Mao_12 predicts the highest C_{SPM} in the turbidity maxima

499   regions and becomes insensitive to C_{SPM} variation from the turbidity front to offshore waters

500   (Fig. 7d). Shen_10 systematically underestimates C_{SPM} in less turbid waters with the derived

501   C_{SPM} generally less than 1 mg/L (Fig. 7f). In contrast to Shen_10, the derived C_{SPM} by the

502   GAA$_{SPM}$ in less turbid waters roughly varies between 0.1 and 20 mg/L (Fig. 7a). The

503   performances by the six algorithms in the Río de La Plata estuary have also been evaluated

504 along a transect highlighted in Fig. 7a. All algorithms, except for the Mao_12, have very

505 comparable C_{SPM} retrievals in moderately turbid waters from P1 to the front of the turbidity

506 plume and then have very different performances in the turbidity maxima zone and relatively

507 clear waters. The discontinuity in C_{SPM} spatial distribution is observed from the mapping

508 products of Shen_10 and GOCI (Fig. 7e and Fig. 7f, respectively), which is also highlighted

509 in Fig. 7g.

510 **4. Discussion**

511 *4.1.   The proposed C_{SPM} retrieval algorithm*

512   The proposed GAA_{SPM} has the overall best performance for the entire C_{SPM} range in this

513 study among all candidate algorithms, which could be attributed to the fact that the GAA_{SPM}

514 takes advantage of the sensitivity of $R_{rs}(\lambda)$ to C_{SPM} in different C_{SPM} ranges. The introduced

515 weighting factors ensure that the generalized index (GI_{SPM}, in Eq. (5)) is dominated by

516 $R_{rs}(671)$ in clear waters and by $R_{rs}(862)$ in highly turbid waters. For instance, as shown in Fig.

517 8, in relatively clear waters where $C_{SPM} < 10$ mg/L, the weighted $R_{rs}(671)$, defined as

518 $c_1 \times W_1 \times R_{rs}(671)$, according to Eq. (5), is about 1 - 2 orders of magnitude larger than the

519 weighted $R_{rs}(745)$ and $R_{rs}(862)$, which are defined as $c_2 \times W_2 \times R_{rs}(745)$ and $c_3 \times W_3 \times R_{rs}(862)$,

520 respectively. Therefore, $R_{rs}(671)$ plays a dominant role in GI_{SPM} for such waters. To the

521 contrary, in highly turbid waters, the weighted $R_{rs}(862)$ is about 1 - 2 orders of magnitude

522 larger than the weighted $R_{rs}(671)$ and $R_{rs}(745)$, and thus dominates the GI_{SPM} in determining

523 C_{SPM}. Therefore, the introduced weighting system can successfully and seamlessly adjust the

524 role of each band to ensure a progressive application of $R_{rs}(\lambda)$ in the longer wavelengths for

525 increasing C_{SPM}, which avoids potential discontinuities in the derived C_{SPM}. More importantly,

526 GAA_{SPM} does not require arbitrary switching boundaries and is, therefore, more applicable for

527 global waters than the hard-wired or blended switching schemes.

528   Although $R_{rs}(745)$ is most sensitive to C_{SPM} in the moderately turbid waters (see Fig. 3a),

529 it appears that the weighted $R_{rs}(745)$ has insignificant contribution to GI_{SPM} for our datasets

530   (see Fig. 8), which could probably be attributed to the fact that a relatively small number of

531   moderately turbid samples were used in the algorithm calibration. Besides, we recalibrated

532   the proposed algorithm without $R_{rs}(745)$ as an input, *i.e.*, a four-band algorithm. Although the

533   performance of the four-band algorithm was only slightly worse than GAA_{SPM} for the entire

534   range (the difference in rMAD is 0.4%), for the moderately turbid waters, rMAD of the

535   derived C_{SPM} is 4.5% larger for the four-band algorithm than GAA_{SPM} (figure not shown here).

536   Therefore, it is necessary to include $R_{rs}(745)$ in the development of a more inclusive dataset

537   for the C_{SPM} algorithm to account for C_{SPM} retrieval in moderately turbid waters.

538   An overall rMAD of 41.3% for GAA_{SPM}-derived C_{SPM} still implies considerable

539   uncertainties of GAA_{SPM} over the entire C_{SPM} range, which is mainly due to the relatively

540   larger uncertainties of the derived C_{SPM} in less turbid waters. Note that rMADs of the derived

541   C_{SPM} by all applicable algorithms in less turbid waters are mostly around 50% - 60%, while

542   rMADs of the retrieved C_{SPM} in highly turbid waters by most algorithms are only around 30%.

543   This relatively poor $R_{rs}(\lambda)$-C_{SPM} relationship in less turbid waters could be explained by many

544   factors. First, the uncertainties of measured $R_{rs}(671)$ in less turbid waters could be relatively

545   large due to the very low values. Also, there might be inconsistency in measured $R_{rs}(\lambda)$

546   among the four *in situ* datasets, due to different instrumentations and correction methods to

547   remove residual surface reflection for the above-water measurements. The uncertainties of

548   measured C_{SPM} could also be relatively large for samples collected from less turbid waters, as

549   fine particles (size < 0.7 μm) were unlikely retained during the filtration due to the use of

550   GF/F filter. On the other hand, in less turbid waters, the C_{SPM}-sensitive $R_{rs}(\lambda)$ shifts to shorter

551   wavelengths, where the absorption coefficients of water components, such as phytoplankton,

552   colored dissolved organic matter, and inorganic matter, have more impacts on the $R_{rs}(\lambda)$

553   variability. In other words, a change in the $R_{rs}(\lambda)$ spectrum in the visible domain is less likely

554   the result of a change in C_{SPM} for such waters. Given that the component absorption

555   coefficients could vary significantly among global oceans, the C_{SPM}-$R_{rs}(\lambda)$ in less turbid

556   waters could be region-dependent. The present results confirm the weak correlation between

557 C_{SPM} and $R_{rs}(\lambda)$ among global measurements (*e.g.*, small R^2 between C_{SPM} and $R_{rs}(\lambda)$ for C_{SPM}

558 < 10 mg/L in Fig. 3a). Nevertheless, compared to the listed algorithms in Section 2.3, the

559 proposed GAA_{SPM} can partly account for the global variability of the $R_{rs}(\lambda)$-C_{SPM} relationship

560 and yields the most accurate retrievals of C_{SPM} for relatively clear waters (Table 6).

561   For turbid waters, C_{SPM} is sensitive to $R_{rs}(\lambda)$ at longer wavelengths, where the particulate

562 backscattering coefficient dominates the variability of $R_{rs}(\lambda)$ as water molecules are the main

563 absorbing component. Thus, much higher R^2 values are found in the $R_{rs}(\lambda)$-C_{SPM} relationships

564 in highly turbid waters (see Fig. 3a). As shown in Table 3, the recalibrated empirical

565 constants are quite comparable with the original ones for the Doxaran_02 algorithm, given

566 that the two sets of empirical constants were calibrated from different datasets. The rMAD of

567 the derived C_{SPM} by Doxaran_02 using their original empirical constants equals to 36.9%

568 (Table 5), while the recalibrated algorithm is slightly improved with rMAD of 31.6 % (Table

569 6). Such findings confirm that a well-calibrated $R_{rs}(\lambda)$-C_{SPM} relationship from highly turbid

570 waters has reduced regional variability, and therefore smaller errors are expected when

571 applying it to very different regions. The reduced regional variability or data dependency of

572 the $R_{rs}(\lambda)$-C_{SPM} relationship in highly turbid waters explains the consistent retrievals from the

573 GAA_{SPM} and other algorithms that employ the $R_{rs}(862)$ in their algorithm's development, such

574 as Dogliotti_15, Shen_10, and Doxaran_02.

575   Although Novoa_17, Dogliotti_15, Han_16, and Mao_12 also allow smooth retrievals for

576 wide-range C_{SPM}, there are important differences between GAA_{SPM} and these algorithms. The

577 Mao_12 is based on a rather complicated proxy and is therefore not easy to be implemented

578 for satellite data, especially when the selected wavelengths for each index (Eqs. (8) - (11))

579 require pre-calibrations and are data dependent. The large uncertainties of Novoa_17 (Fig. 4b)

580 could be expected as Novoa_17 simply employs linear relationships between C_{SPM} and

581 reflectance at the green and red bands to calculate the C_{SPM_Green} and C_{SPM_Red} (see Table 4),

582 respectively, while such relationships are supposed to be region dependent (see Fig. 3a). Also,

583 for Novoa_17, Dogliotti_15, and Han_16, they all employ switching boundaries in their

584   algorithms, which could result in significant uncertainties for samples that were wrongly

585   classified by the switching boundaries. Take Dogliotti_15 for example, in our *in situ* datasets,

586   19 samples with $\rho_w(671) > 0.07$ have C_{SPM} less than 50 mg/L. The switching scheme of

587   Dogliotti_15 will employ $\rho_w(862)$ to derive C_{SPM} for these 19 samples and results in an rMAD

588   of 187.1%. The wrong classification by the boundaries could partly explain why there are

589   'outliers' in the validation results of Novoa_17 (Fig. 4b), Dogliotti_15 (Fig. 4c), and Han_16

590   (Fig. 4d). The switch scheme of GAA$_{SPM}$, on the other hand, is based on the relative value of

591   $R_{rs}(\lambda)$, instead of using a single band $R_{rs}(\lambda)$. Thus, GAA$_{SPM}$ could effectively reduce the

592   presence of such outliers. More importantly, the selected boundaries for relatively clear

593   waters in Novoa_17, Dogliotti_15, and Han_16 were all from their respective study regions.

594   However, the designated boundaries differed largely from $\rho_w(671) = 0.05$ to $\rho_w(671) = 0.094$,

595   suggesting the saturation of $\rho_w(671)$ to the level of C_{SPM} could be region dependent (Shi and

596   Wang, 2014). In this study, it appears that the boundary adopted in Dogliotti_15 works the

597   best for our datasets, but such selection could fail for the calibration datasets in Novoa et al.

598   (2017) and Han et al. (2016). Therefore, it is important to obtain a unified boundary for global

599   applications for such type of algorithms. GAA$_{SPM}$, on the other hand, could be globally

600   applicable, given that it does not require any hard switching boundaries.

601   *4.2.   Sensitivity of the derived C_{SPM} to uncertainties of $R_{rs}(NIR)$*

602   Measured $R_{rs}(\lambda)$ at the NIR bands, by field instruments or satellite sensors, are always

603   subject to uncertainties due to low signals in these wavelengths, especially for relatively clear

604   waters. Validation of the NIR-SWIR atmospherically corrected $R_{rs}(\lambda)$ in Fig. 5 also shows

605   that there might be relatively larger uncertainties of $R_{rs}(NIR)$ from VIIRS-SNPP. Therefore,

606   the sensitivity of the GAA$_{SPM}$ to the uncertainties of $R_{rs}(NIR)$ needs to be assessed, especially

607   when the uncertainties of satellite-measured $R_{rs}(NIR)$ could be high and are not well known.

608   It should be noted that large uncertainties may also come from *in situ $R_{rs}(NIR)$* measurements,

609   particularly for the relatively clear waters with very small $R_{rs}(NIR)$ values.

610   Tests were carried out for the VIIRS-SNPP image used in Fig. 6 with systematic errors

611   of ±10% and ±20% added to the two NIR bands at 745 and 862 nm, respectively. These error-

612   included VIIRS-SNPP images were then employed to derive C_{SPM} using GAA$_{SPM}$. Fig. 9

613   shows the density scatter plots to present the comparisons between the originally derived C_{SPM}

614   and the derived C_{SPM} from the error-included images. Statistical results are given for less

615   turbid and highly turbid waters, respectively, to better demonstrate the impact of $R_{rs}(NIR)$

616   uncertainties on the C_{SPM} retrieval for waters with different C_{SPM} ranges.

617   As shown in Fig. 9, uncertainties of $R_{rs}(NIR)$ have negligible impacts on retrieved C_{SPM}

618   for less turbid waters. A maximum of 20% error added to both $R_{rs}(745)$ and $R_{rs}(862)$ only

619   results in less than 2% in the derived C_{SPM} for waters with $C_{SPM} < 50$ mg/L, which is because

620     $R_{rs}(671)$ is often 1 - 2 orders of magnitude larger than those of $R_{rs}(NIR)$ in less turbid waters.

621   Even with 40% error for the two NIR bands, $R_{rs}(671)$ still contributes the most weight to the

622   *GI_{SPM}* for $C_{SPM} < 50$ mg/L.

623   For turbid waters, the derived C_{SPM} is more sensitive to the uncertainties of $R_{rs}(NIR)$, but

624   overall has smaller or equivalent errors to the errors added to $R_{rs}(NIR)$. As shown in Fig. 9a,

625   a total of −40% error introduced to $R_{rs}(745)$ and $R_{rs}(862)$ results in an rMAD of 28.5% for the

626   derived C_{SPM}, while a +40% error of $R_{rs}(NIR)$ results in an rMAD of 38.2% for the derived

627   C_{SPM}. In both cases, the errors of the derived C_{SPM} are smaller than the errors added to

25

628 R_{rs}(NIR). Considering most atmospheric correction algorithms tend to underestimate R_{rs}(NIR),

629 instead of the other way around, satellite-derived C_{SPM} by GAA$_{SPM}$ is expected to be relatively

630 noise-tolerant to the underestimation of R_{rs}(NIR) by the atmospheric correction.

631 **5. Conclusions**

632 In this study, we proposed an empirical algorithm that allows effective and seamless

633 retrieval of C_{SPM} from ocean color across ocean to highly turbid river mouths, where existing

634 algorithms in the literature will generally result in either unjustified numerical discontinuities

635 or larger uncertainties. Validation of GAA$_{SPM}$ and inter-comparison with existing algorithms

636 (after recalibration with the datasets of this study) give confidence to the application of

637 GAA$_{SPM}$ over regions with a wide range of C_{SPM}. Given that the GAA$_{SPM}$ is calibrated based

638 on data collected from multiple estuarine and coastal regions around the world, GAA$_{SPM}$

639 shows a feature of global applicability, which is essential to generate C_{SPM} maps from satellite

640 ocean color sensors. Demonstrations using VIIRS-SNPP images over two turbid river mouths

641 were presented, where GAA$_{SPM}$ produced reasonable C_{SPM} maps in terms of both the range of

642 the derived C_{SPM} and the spatial distribution pattern. Since there are many operational satellite

643 ocean color sensors that have similar band configurations as VIIRS in the visible-NIR

644 domains, GAA$_{SPM}$ could be easily adapted to those satellite data after mild sensor-based

645 adjustments to produce global C_{SPM} maps with improved spatial-temporal resolution through

646 merging of multi-sensor data.

647

664 **Appendix 1. Interpolation of the measured $R_{rs}(\lambda)$ for the COASTLOOC dataset**

665   Absorption by pure water dominates the total absorption coefficients at NIR bands in

666 offshore waters and open oceans. To obtain accurate $R_{rs}(\lambda)$ at 745 nm and construct a

667 reasonable spectral feature at the NIR bands for the COASTLOOC dataset from the measured

668 $R_{rs}(\lambda)$ at the twelve wavelengths (see Table 1), a semi-analytical interpolation approach is

669 employed.

670   Non-water absorption and backscattering coefficients (a_{nw} and b_{bp}, in m^{-1}) are first derived

671 from measured $R_{rs}(\lambda)$ at the twelve COASTLOOC wavelengths using the quasi-analytical

672 algorithm (QAA) (Lee et al., 2002). The derived a_{nw} is then linearly interpolated to

673 hyperspectral data from 411 to 866 nm with an increment of 1 nm. The derived b_{bp} is

674 interpolated to the same wavelength range following the parameterization of b_{bp} in QAA.

675 Given that absorption and backscattering coefficients of pure water (a_w and b_{bw}) are known

676 (Kou et al., 1993; Morel, 1974; Pope and Fry, 1997), hyperspectral total absorption and

677 backscattering coefficients ($a(\lambda)$ and $b_b(\lambda)$) are estimated by,

$$a(\lambda) = a_{nw}(\lambda) + a_w(\lambda) \tag{A1}$$

$$b_b(\lambda) = b_{bp}(\lambda) + b_{bw}(\lambda) \tag{A2}$$

678   Hyperspectral $R_{rs}(\lambda)$ can be finally determined from $a(\lambda)$ and $b_b(\lambda)$ following,

$$r_{rs}(\lambda) = g_0 \left(\frac{b_b}{b_b + a} \right) + g_1 \left(\frac{b_b}{b_b + a} \right)^2 \tag{A3}$$

$$R_{rs}(\lambda) = 0.52 r_{rs}(\lambda) / (1 - 1.7 r_{rs}(\lambda)) \tag{A4}$$

679   where $r_{rs}(\lambda)$ is the remote sensing reflectance beneath the surface with $g_0 = 0.089$ and $g_1 =$

680   0.125 (Gordon et al., 1988; Lee et al., 1999).

681   Using QAA for the retrieval of a_{nw} and b_{bp}, instead of inversion algorithms using spectral

682   optimization, would ensure the interpolated $R_{rs}(\lambda)$ matches the measured $R_{rs}(\lambda)$ exactly at the

683   twelve COASTLOOC wavelengths. To evaluate the performance of the semi-analytical

684   interpolation approach, measured $R_{rs}(\lambda)$ of the UMB dataset was first resampled to the twelve

685   COASTLOOC wavelengths, and $R_{rs}(745)$ was then estimated from the above described semi-

686   analytical interpolation, as well as from the linear interpolation between $R_{rs}(705)$ and $R_{rs}(779)$.

687   Fig. A1 shows a comparison of estimated $R_{rs}(745)$ by the two interpolation methods, which

688   demonstrates that the semi-analytical approach can provide much more consistent estimations

689   of $R_{rs}(745)$ than the linear interpolation method.

690
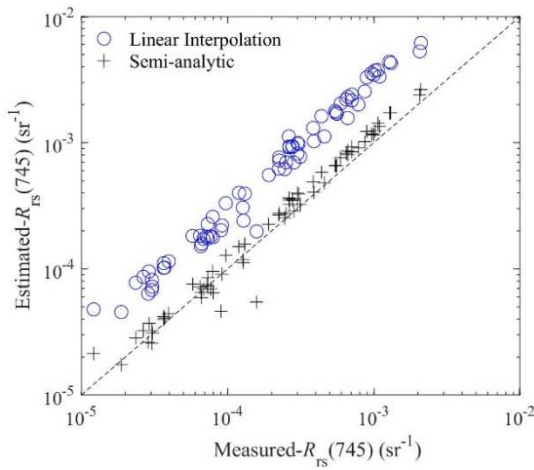
691   Fig. A1. Evaluation of the interpolated $R_{rs}(\lambda)$ at 745 nm by the linear and the semi-analytic approaches,
692   using the UMB dataset as an example.

693

694   **References**

695   Austin, R. W. (1974). Inherent spectral radiance signatures of the ocean surface, p. 2.1–2.20. *In* Ocean
696   Color Analysis, Scripps Institution of Oceanography, San Diego, CA.

697   Babin, M., Stramski, D., Ferrari, G.M., Claustre, H., Bricaud, A., Obolensky, G., & Hoepffner, N.
698   (2003). Variations in the light absorption coefficients of phytoplankton, nonalgal particles, and

699   dissolved organic matter in coastal waters around Europe. *Journal of Geophysical Research-*
700   *Oceans*, 108, 3211.

701   Binding, C., Bowers, D., & Mitchelson-Jacob, E. (2005). Estimating suspended sediment
702   concentrations from ocean colour measurements in moderately turbid waters; the impact of
703   variable particle scattering properties. *Remote Sensing of Environment*, 94, 373-383.

704   D'Sa, E.J., Miller, R.L., & McKee, B.A. (2007). Suspended particulate matter dynamics in coastal
705   waters from ocean color: Application to the northern Gulf of Mexico. *Geophysical Research*
706   *Letters*, 34, L23611.

707   Dogliotti, A., Ruddick, K.G., Nechad, B., Doxaran, D., & Knaeps, E. (2015). A single algorithm to
708   retrieve turbidity from remotely-sensed data in all coastal and estuarine waters. *Remote Sensing of*
709   *Environment*, 156, 157-168.

710   Doxaran, D., Cherukuru, N., & Lavender, S.J. (2006). Apparent and inherent optical properties of
711   turbid estuarine waters: measurements, empirical quantification relationships, and modeling.
712   *Applied Optics*, 45, 2310-2324.

713   Doxaran, D., Froidefond, J.-M., Lavender, S., & Castaing, P. (2002a). Spectral signature of highly
714   turbid waters: Application with SPOT data to quantify suspended particulate matter concentrations.
715   *Remote Sensing of Environment*, 81, 149-161.

716   Doxaran, D., Froidefond, J.M., & Castaing, P. (2002b). A reflectance band ratio used to estimate
717   suspended matter concentrations in sediment-dominated coastal waters. *International Journal of*
718   *Remote Sensing*, 23, 5079-5085.

719   Doxaran, D., Froidefond, J.M., & Castaing, P. (2003). Remote-sensing reflectance of turbid sediment-
720   dominated waters. Reduction of sediment type variations and changing illumination conditions
721   effects by use of reflectance ratios. *Applied Optics*, 42, 2623-2634.

722   Fargion, G.S., & Mueller, J.L. (2000). *Ocean optics protocols for satellite ocean color sensor*
723   *validation, Revision 2*. National Aeronautics and Space Administration, Goddard Space Flight
724   Center.

725   Freeman, L.A., Ackleson, S.G., & Rhea, W.J. (2017). Comparison of remote sensing algorithms for
726   retrieval of suspended particulate matter concentration from reflectance in coastal waters. *Journal*
727   *of Applied Remote Sensing*, 11, 046028.

728   Gohin, F., Druon, J., & Lampert, L. (2002). A five channel chlorophyll concentration algorithm applied
729   to SeaWiFS data processed by SeaDAS in coastal waters. *International Journal of Remote Sensing*,
730   23, 1639-1661.

731   Gohin, F., Loyer, S., Lunven, M., Labry, C., Froidefond, J.-M., Delmas, D., Huret, M., & Herbland, A.
732   (2005). Satellite-derived parameters for biological modelling in coastal waters: Illustration over the
733   eastern continental shelf of the Bay of Biscay. *Remote Sensing of Environment*, 95, 29-46.

734   Gordon, H.R., Brown, O.B., Evans, R.H., Brown, J.W., Smith, R.C., Baker, K.S., & Clark, D.K. (1988).
735   A Semianalytic Radiance Model of Ocean Color. *Journal of Geophysical Research-Atmospheres*,
736   93, 10909-10924.

737   Gordon, H.R., & Wang, M. (1994). Retrieval of water-leaving radiance and aerosol optical thickness
738   over the oceans with SeaWiFS: a preliminary algorithm. *Applied Optics*, 33, 443-452.

739   He, X., Bai, Y., Pan, D., Huang, N., Dong, X., Chen, J., Chen, C.-T.A., & Cui, Q. (2013). Using
740   geostationary satellite ocean color data to map the diurnal dynamics of suspended particulate
741   matter in coastal waters. *Remote Sensing of Environment*, 133, 225-239.

742   IOCCG (2000). Remote Sensing of Ocean Colour in Coastal, and Other Optically-Complex, Waters.
743   *Sathyendranath, S. (ed.), Reports of the International Ocean-Colour Coordinating Group*, No.3,
744   IOCCG, Dartmouth, Canada.

745   IOCCG (2006). Remote Sensing of Inherent Optical Properties: Fundamentals,Tests of Algorithms,
746   and Applications. *Lee, Z. P. (ed.), Reports of the International Ocean-Colour Coordinating Group*,
747   No. 5, IOCCG, Dartmouth, Canada.

748 Jiang, L., & Wang, M. (2014). Improved near-infrared ocean reflectance correction algorithm for
749   satellite ocean color data processing. *Optics Express*, 22, 21657-21678.

750 Knaeps, E., Doxaran, D., Dogliotti, A., Nechad, B., Ruddick, K., Raymaekers, D., & Sterckx, S. (2018).
751   The SeaSWIR dataset. *Earth System Science Data*, 10, 1439-1449.

752 Knaeps, E., Ruddick, K., Doxaran, D., Dogliotti, A., Nechad, B., Raymaekers, D., & Sterckx, S. (2015).
753   A SWIR based algorithm to retrieve total suspended matter in extremely turbid waters. *Remote*
754   *Sensing of Environment*, 168, 66-79.

755 Kou, L., Labrie, D., & Chylek, P. (1993). Refractive indices of water and ice in the 0.65-to 2.5-μm
756   spectral range. *Applied Optics*, 32, 3531-3540.

757 Laws, E.A. (1997). *Mathematical methods for oceanographers: An introduction*. John Wiley & Sons.

758 Lee, Z., Carder, K.L., Mobley, C.D., Steward, R.G., & Patch, J.S. (1999). Hyperspectral remote
759   sensing for shallow waters. 2. Deriving bottom depths and water properties by optimization.
760   *Applied Optics*, 38, 3831-3843.

761 Lee, Z., Pahlevan, N., Ahn, Y.-H., Greb, S., & O'Donnell, D. (2013). Robust approach to directly
762   measuring water-leaving radiance in the field. *Applied Optics*, 52, 1693-1701.

763 Lee, Z.P., Carder, K.L., & Arnone, R.A. (2002). Deriving inherent optical properties from water color:
764   a multiband quasi-analytical algorithm for optically deep waters. *Applied Optics*, 41, 5755-5772.

765 Loisel, H., Mangin, A., Vantrepotte, V., Dessailly, D., Dinh, D.N., Garnesson, P., Ouillon, S., Lefebvre,
766   J.-P., Mériaux, X., & Phan, T.M. (2014). Variability of suspended particulate matter concentration
767   in coastal waters under the Mekong's influence from ocean color (MERIS) remote sensing over the
768   last decade. *Remote Sensing of Environment*, 150, 218-230.

769 Loisel, H., & Morel, A. (2001). Non-isotropy of the upward radiance field in typical coastal (Case 2)
770   waters. *International Journal of Remote Sensing*, 22, 275-295.

771 Luo, Y., Doxaran, D., Ruddick, K., Shen, F., Gentili, B., Yan, L., & Huang, H. (2018). Saturation of
772   water reflectance in extremely turbid media based on field measurements, satellite data and bio-
773   optical modelling. *Optics Express*, 26, 10435-10451.

774 Mao, Z., Chen, J., Pan, D., Tao, B., & Zhu, Q. (2012). A regional remote sensing algorithm for total
775   suspended matter in the East China Sea. *Remote Sensing of Environment*, 124, 819-831.

776 Min, J., Choi, J., Park, Y., & Ryu, J. (2013). Retrieval of suspended sediment concentration in the
777   coastal waters of Yellow Sea from Geostationary Ocean Color Imager (GOCI). In, *Proc. of*
778   *International Symposium on Remote Sensing* (pp. 809-912).

779 Mobley, C.D. (1999). Estimation of the remote-sensing reflectance from above-surface measurements.
780   *Applied Optics*, 38, 7442-7455.

781 Morel, A. (1974). Optical properties of pure water and pure sea water. *Optical aspects of*
782   *Oceanography*, 1-24.

783 Nechad, B., Ruddick, K., & Park, Y. (2010). Calibration and validation of a generic multisensor
784   algorithm for mapping of total suspended matter in turbid waters. *Remote Sensing of Environment*,
785   114, 854-866.

786 Novoa, S., Doxaran, D., Ody, A., Vanhellemont, Q., Lafon, V., Lubac, B., & Gernez, P. (2017).
787   Atmospheric corrections and multi-conditional algorithm for multi-sensor remote sensing of
788   suspended particulate matter in low-to-high turbidity levels coastal waters. *Remote Sensing*, 9, 61.

789 Pope, R.M., & Fry, E.S. (1997). Absorption spectrum (380 –700 nm)of pure water. II. Integrating
790   cavity measurements. *Applied Optics*, 36, 8710-8723.

791 Ruddick, K.G., De Cauwer, V., Park, Y.-J., & Moore, G. (2006). Seaborne measurements of near
792   infrared water‐leaving reflectance: The similarity spectrum for turbid waters. *Limnology and*
793   *Oceanography*, 51, 1167-1179.

794 Seegers, B.N., Stumpf, R.P., Schaeffer, B.A., Loftin, K.A., & Werdell, P.J. (2018). Performance
795   metrics for the assessment of satellite data products: an ocean color case study. *Optics Express*, 26,
796   7404-7422.

797 Shang, Z., Lee, Z., Dong, Q., & Wei, J. (2017). Self-shading associated with a skylight-blocked
798   approach system for the measurement of water-leaving radiance and its correction. *Applied Optics*,
799   56, 7033-7040.

800 Shen, F., Salama, M.S., Zhou, Y.X., Li, J.F., Su, Z.B., & Kuang, D.B. (2010a). Remote-sensing
801   reflectance characteristics of highly turbid estuarine waters - a comparative experiment of the
802   Yangtze River and the Yellow River. *International Journal of Remote Sensing*, 31, 2639-2654.

803 Shen, F., Verhoef, W., Zhou, Y.X., Salama, M.S., & Liu, X.L. (2010b). Satellite Estimates of Wide-
804   Range Suspended Sediment Concentrations in Changjiang (Yangtze) Estuary Using MERIS Data.
805   *Estuaries and Coasts*, 33, 1420-1429.

806 Shen, F., Zhou, Y.X., Li, J.F., He, Q., & Verhoef, W. (2013). Remotely sensed variability of the
807   suspended sediment concentration and its response to decreased river discharge in the Yangtze
808   estuary and adjacent coast. *Continental Shelf Research*, 69, 52-61.

809 Shen, F., Zhou, Y.X., Peng, X.Y., & Chen, Y.L. (2014). Satellite multi-sensor mapping of suspended
810   particulate matter in turbid estuarine and coastal ocean, China. *International Journal of Remote
811   Sensing*, 35, 4173-4192.

812 Shi, W., & Wang, M. (2014). Ocean reflectance spectra at the red, near-infrared, and shortwave
813   infrared from highly turbid waters: A study in the Bohai Sea, Yellow Sea, and East China Sea.
814   *Limnology and Oceanography*, 59, 427-444.

815 Shi, W., & Wang, M. (2007). Detection of turbid waters and absorbing aerosols for the MODIS ocean
816   color data processing. *Remote Sensing of Environment*, 110, 149-161.

817 Shi, W., Zhang, Y., & Wang, M. (2018). Deriving Total Suspended Matter Concentration from the
818   Near-Infrared-Based Inherent Optical Properties over Turbid Waters: A Case Study in Lake Taihu.
819   *Remote Sensing*, 10, 333.

820 Siswanto, E., Tang, J., Yamaguchi, H., Ahn, Y.-H., Ishizaka, J., Yoo, S., Kim, S.-W., Kiyomoto, Y.,
821   Yamada, K., & Chiang, C. (2011). Empirical ocean-color algorithms to retrieve chlorophyll-a,
822   total suspended matter, and colored dissolved organic matter absorption coefficient in the Yellow
823   and East China Seas. *Journal of Oceanography*, 67, 627.

824 Volpe, V., Silvestri, S., & Marani, M. (2011). Remote sensing retrieval of suspended sediment
825   concentration in shallow waters. *Remote Sensing of Environment*, 115, 44-54.

826 Wang, M. (2007). Remote sensing of the ocean contributions from ultraviolet to near-infrared using the
827   shortwave infrared bands: simulations. *Applied Optics*, 46, 1535-1547.

828 Wang, M., & Shi, W. (2007). The NIR-SWIR combined atmospheric correction approach for MODIS
829   ocean color data processing. *Optics Express*, 15, 15722-15733.

830 Wang, M., Shi, W., & Tang, J. (2011). Water property monitoring and assessment for China's inland
831   Lake Taihu from MODIS-Aqua measurements. *Remote Sensing of Environment*, 115, 841-854.

832 Wang, M., Tang, J., & Shi, W. (2007). MODIS‐derived ocean color products along the China east
833   coastal region. *Geophysical Research Letters*, 34.

834 Zhang, M., Tang, J., Dong, Q., Song, Q., & Ding, J. (2010). Retrieval of total suspended matter
835   concentration in the Yellow and East China Seas from MODIS imagery. *Remote Sensing of
836   Environment*, 114, 392-403.

837 Zhang, T., & Fell, F. (2007). An empirical algorithm for determining the diffuse attenuation coefficient
838   K-d in clear and turbid waters from spectral remote sensing reflectance. *Limnology and
839   Oceanography-Methods*, 5, 457-462.
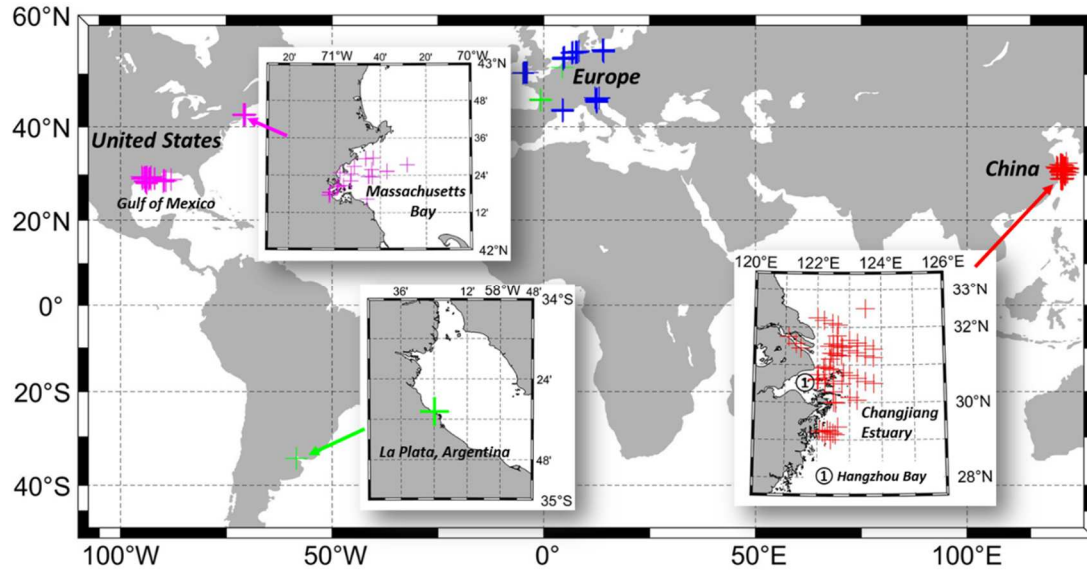
840

841

Figures and tables

843

844 Fig. 1. Sampling locations of the four *in situ* datasets. The red, green, magenta, and blue crosses
845 represent the Changjiang, the SeaSWIR, the UMB, and the COASTLOOC datasets, respectively. Three
846 insert figures zoom in the sampling locations in the Massachusetts Bay, the Río de La Plata estuary,
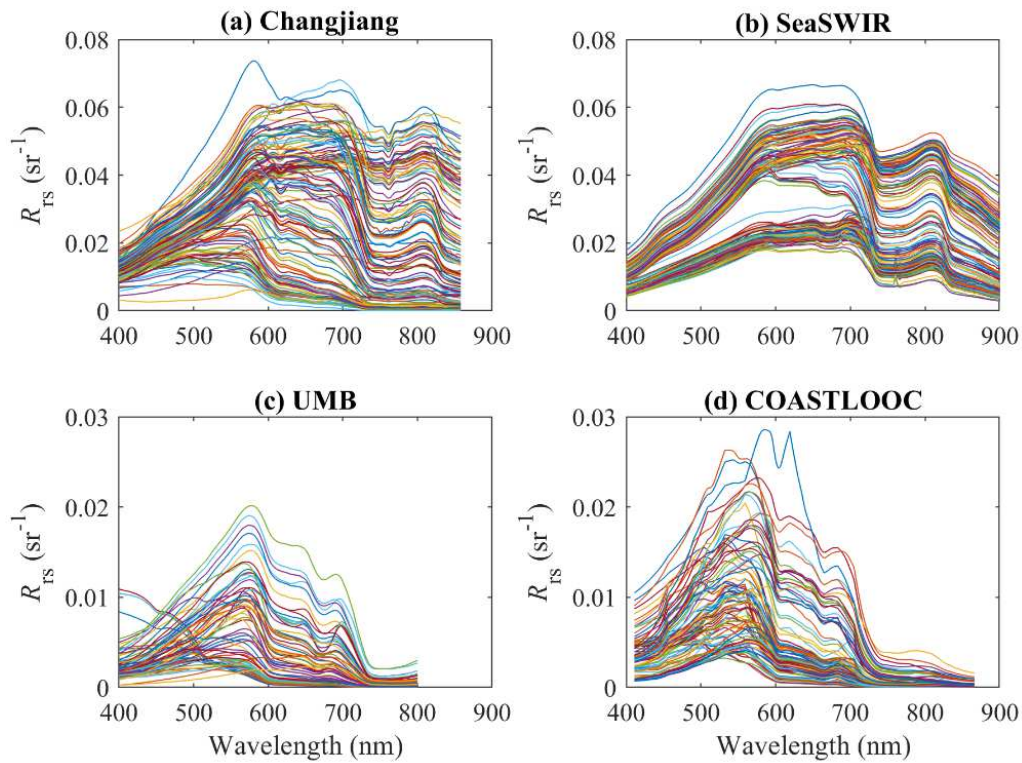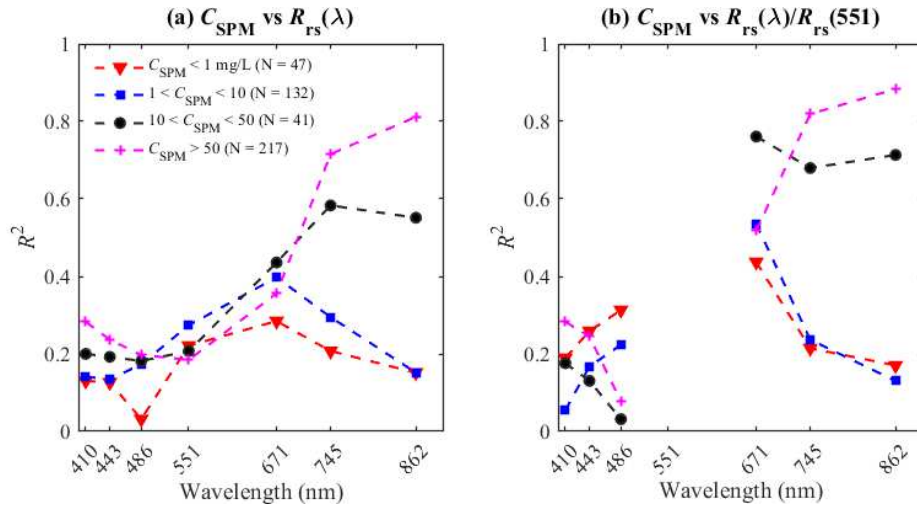847 and the Changjiang estuary, respectively.

848

849

850 Fig. 2. Measured $R_{rs}(\lambda)$ spectra of the Changjiang (a), the SeaSWIR (b), the UMB (c), and the
851 COASTLOOC (d) datasets.

852

853

854

Fig. 3. The determination coefficient (R^2) between C_{SPM} and R_{rs} measurements for separate C_{SPM}
ranges. (a) R^2 between C_{SPM} and $R_{rs}(\lambda)$ at a single VIIRS band. (b) R^2 between C_{SPM} and the band ratios
of $R_{rs}(\lambda)$ over $R_{rs}(551)$.

858

859
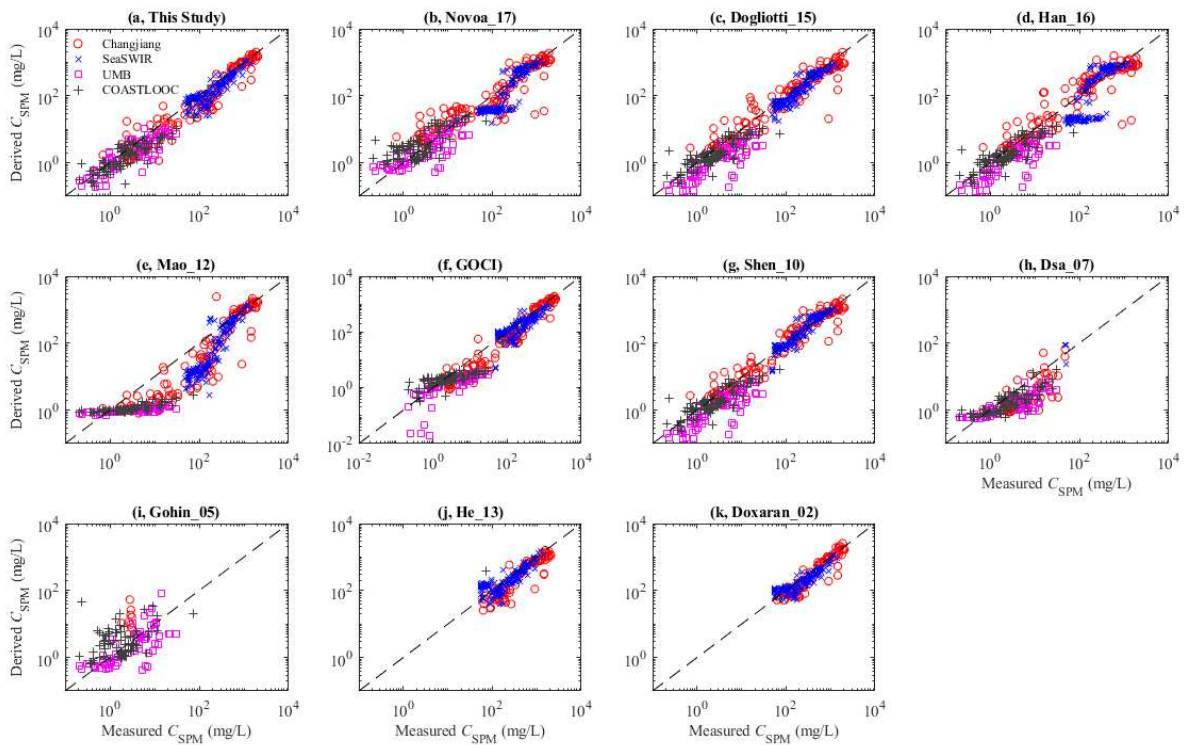
Fig. 4. Validation and inter-comparison of C_{SPM} retrieval algorithms. Panels (h) and (i) present the
validation results of Dsa_07 and Gohin_05 for C_{SPM} < 50 mg/L, while panels (j) and (k) show the
validation results of He_13 and Doxaran_02 for C_{SPM} > 50 mg/L.

863
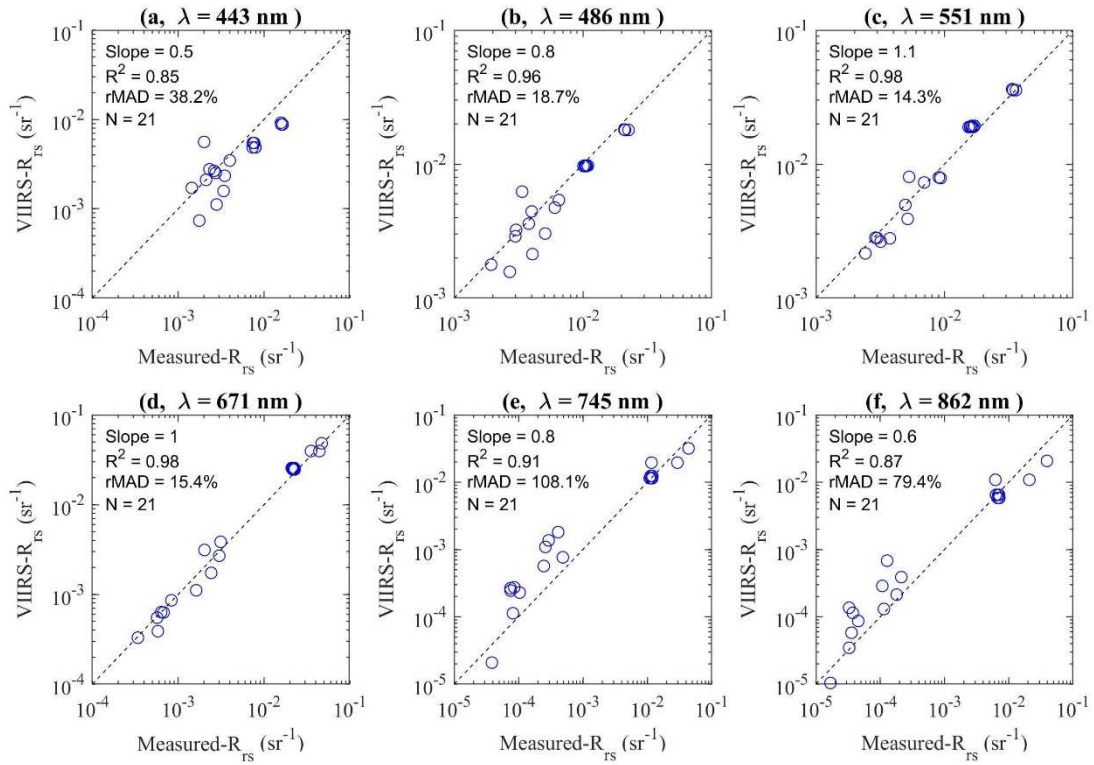
Fig. 5. Validation of VIIRS NIR-SWIR $R_{rs}(\lambda)$ product against field measurements collected within 1
hour of the acquisition of the VIIRS image.

866

867
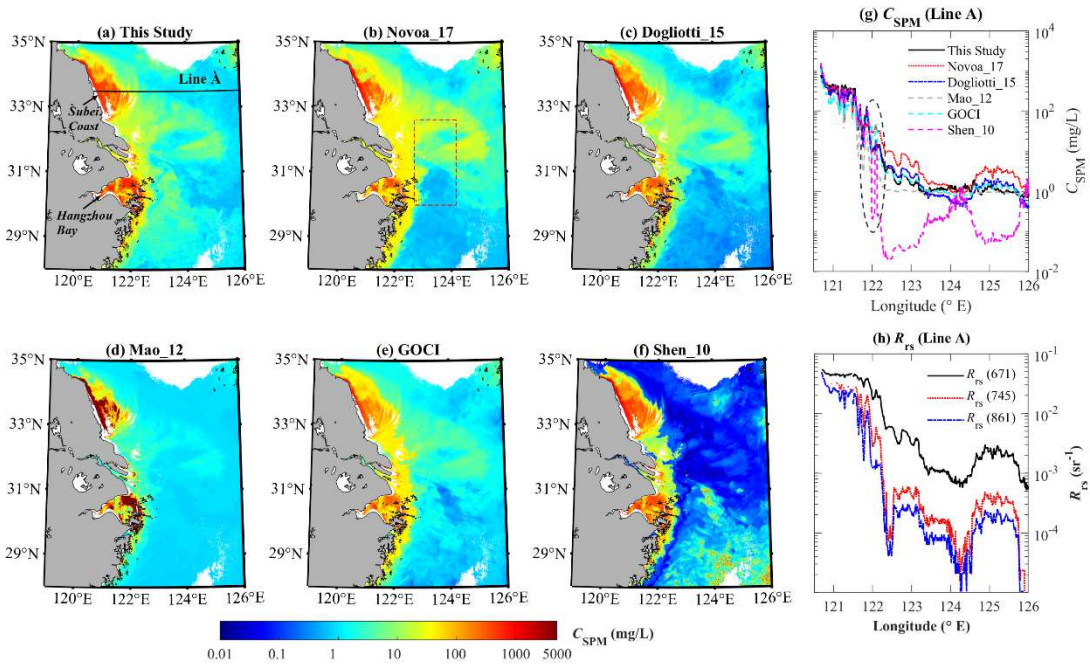
Fig. 6. VIIRS-SNPP C_{SPM} mapping products over the Changjiang estuarine and coastal waters derived
by GAA$_{SPM}$ (a), Novoa_17 (b), Dogliotti_15 (c), Mao_12 (d), GOCI (e), and Shen_10 (f), respectively.
Variations of the derived C_{SPM} from the six algorithms and the VIIRS $R_{rs}(\lambda)$ at 671, 745, and 861 nm

871   along a transect (Lines A in panel (a)) are presented in panels (g) and (h), respectively. Derived C_{SPM}

872   over 5000 mg/L by Mao_12 is not shown in panel (g). The VIIRS-SNPP data is merged from two

873   images acquired at 04:44:20 UTC and 04:45:46 UTC on April 8, 2018.

874

875
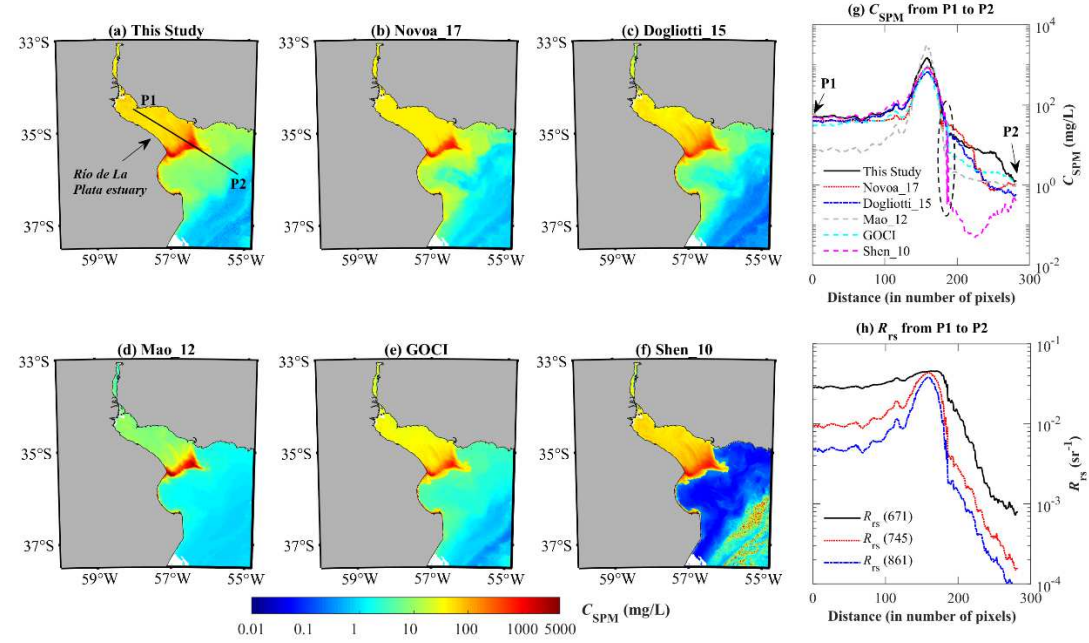
876   Fig. 7. Same as Fig. 6, but for C_{SPM} mapping products over the Río de La Plata estuary of Argentina.

877   Panels (g) and (h) show the variation of the derived C_{SPM} by the six algorithms and VIIRS $R_{rs}(\lambda)$ at 671,

878   745, and 861 nm along the transection from P1 to P2 in panel (a). The VIIRS-SNPP data is merged

879   from two images acquired at 18:10:12 UTC and 18:11:37 UTC on November 25, 2017.

880

881
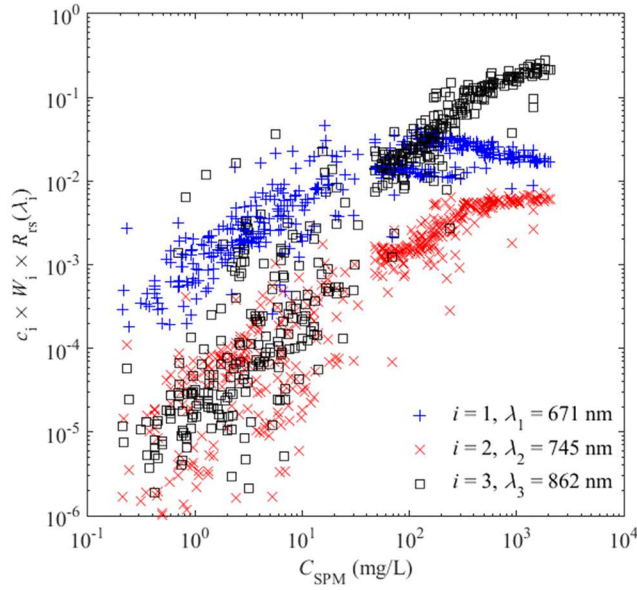
Fig. 8. The contribution of weighted $R_{rs}(\lambda)$ (denoted as $c_i \times W_i \times R_{rs}(\lambda_i)$ in Eq. (5)) at λ_1 (671), λ_2 (745), and λ_3 (862) to the GI_{SPM} with respect to increasing C_{SPM}. The scatter plots are based on the four *in situ* datasets.
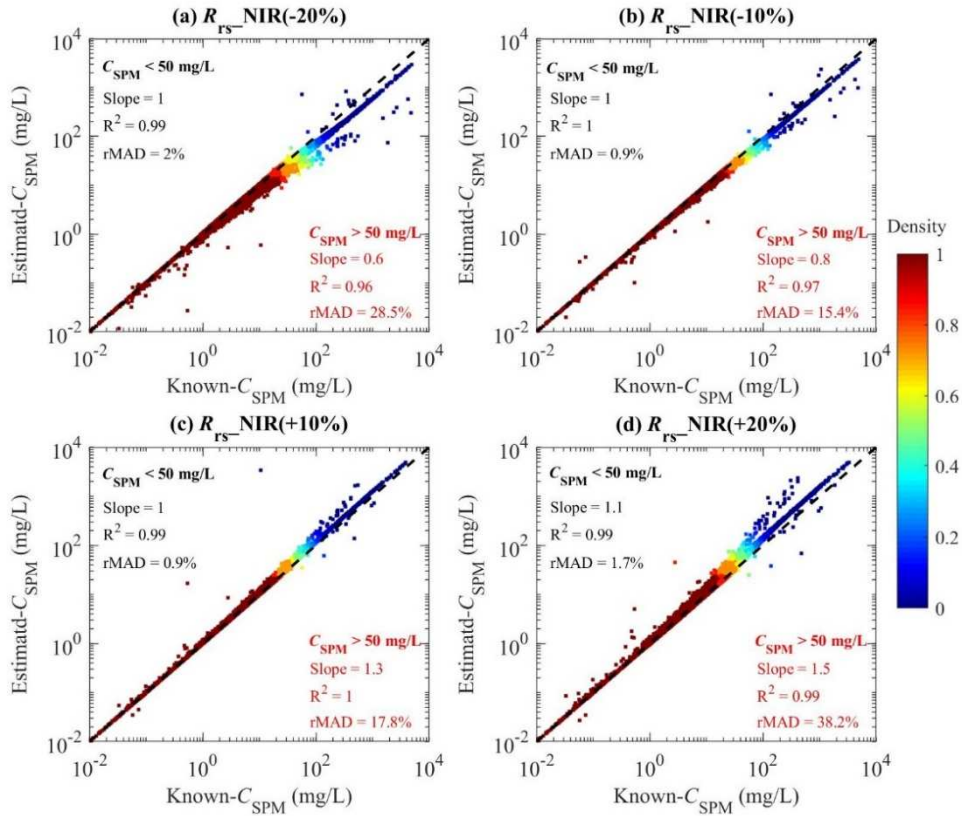

885

Fig. 9. Sensitivity analysis of GAA_{SPM} with respect to introduced error ($\pm 10\%$ and $\pm 20\%$) to $R_{rs}(\lambda)$ at two VIIRS NIR bands. The density scatters plots are based on the same VIIRS-SNPP image used in Fig. 6, with the known-C_{SPM} derived from the original VIIRS-SNPP data and the estimated-C_{SPM} derived from the error-included data.

890

Table 1. Brief descriptions and overview of the four *in situ* datasets collected from multiple estuarine and coastal areas.

Datasets	SPM range (Mean) (mg/L)	R_{rs} Spectral range (nm)	No.	Instrument	Sampling Dates	Sampling Regions
Changjiang	0.7 - 2068.8 (412.4)	350 - 858	130	HyperSAS	Feb, Jun 2011, Mar 2013	Changjiang River and Estuary
SeaSWIR	48.3 - 1400.5 (275.1)	350 - 1300	137	ASD	Oct 2010 - Aug 2013	Scheldt River, Gironde River, Río de La Plata
UMB	0.2 - 30.6 (5.7)	350 - 800	71	RISBA	Sep 2013, Jun - Nov 2018	Gulf of Mexico, Massachusetts Bay
COASTLOOC	0.7 - 72.8 (4.8)	411, 443, 456, 490, 509, 532, 619, 665, 683, 705, 779, 866	99	NA*	Apr 1997 - Sep 1998	European coastal waters

* NA indicates no information available or not applicable.

Table 2. Empirical coefficients of the proposed GAA$_{SPM}$ calibrated by the four *in situ* datasets.

Coefficients	a_1 (mg/L)	a_2	c_0	c_1	c_2	c_3
Values	20.43	2.15	0.04	1.17	0.4	14.86

Table 3. Quantitative C_{SPM} retrieval algorithms from peer-reviewed articles.

Algorithm	Original	Recalibrated	Remarks
Dsa_07	$C_{SPM}=10\wedge(1.25+1.11\times\log10(X))$	$C_{SPM}=10\wedge(-0.44+1.93\times\log10(X))$	$X=R_{rs}(671)/R_{rs}(551)$
He_13	$C_{SPM}=10\wedge(1.076+1.123\ X)$	$C_{SPM}=10\wedge(1.14+0.92\ X)$	$X=R_{rs}(745)/R_{rs}(486)$
Doxaran_02	$C_{SPM}=\exp(3.132\ X+3.01)$	$C_{SPM}=\exp(2.8\ X+3.53)$	$X=R_{rs}(862)/R_{rs}(551)$
GOCI	$C_{SPM}=10\wedge(0.088+1.627\ X1+1.121\ X2)$	$C_{SPM}=10\wedge(1.92+1.35\ X1-0.26\ X2)$	$C_{SPM}\geq 50$ mg/L $X1=R_{rs}(745)/R_{rs}(551)$ $X2=R_{rs}(671)/R_{rs}(486)$
GOCI	$C_{SPM}=10\wedge(0.649+25.623\ X1-0.646\ X2)$	$C_{SPM}=10\wedge(0.59+13.5\ X1-0.66\ X2)$	$C_{SPM} < 50$ mg/L $X1=R_{rs}(551)+R_{rs}(671)$ $X2=R_{rs}(486)/R_{rs}(551)$
Shen_10	$C_{SPM}=2\times0.078\ X/(10.629\times(0.078-X)^2)$	$C_{SPM}=2\times7.75\ X/(0.0004\times(7.75-X)^2)$	$C_{SPM} < 50$ mg/L $X=R_{rs}(671)$
Shen_10	$C_{SPM}=2\times0.104\ X/(1.804\times(0.104-X)^2)$	$C_{SPM}=2\times0.11\ X/(0.002\times(0.11-X)^2)$	$C_{SPM}\geq 50$ mg/L $X=R_{rs}(862)$

905 Table 4. The multi-conditional Novoa_17 algorithm for C_{SPM} retrieval. The weighting factors (α_{1-2} and
906 β_{1-2}) for $C_{\text{SPM\_Green-Red}}$ and $C_{\text{SPM\_Red-NIR}}$ are calculated following Eqs. (19) - (20) in the text.

ρ_w (671) values	SPM algorithm	Expressions	
		Original	Recalibrated
<0.007	$C_{\text{SPM\_Green}}$	$96.6\ \rho_w(551)$	$93.5\ \rho_w(551)$
(0.007;0.016)	$C_{\text{SPM\_Green-Red}}$	$\alpha_1\ C_{\text{SPM\_Green}} + \beta_1\ C_{\text{SPM\_Red}}$	
(0.016;0.08)	$C_{\text{SPM\_Red}}$	$575.8\ \rho_w(671)$	$529.3\ \rho_w(671)$
(0.08;0.12)	$C_{\text{SPM\_Red-NIR}}$	$\alpha_2\ C_{\text{SPM\_Red}} + \beta_2\ C_{\text{SPM\_NIR}}$	
>0.12	$C_{\text{SPM\_NIR}}$	$32110\ \rho_w(862)^2 + 2204\ \rho_w(862)$	$73489\ \rho_w(862)^2 - 1389.5\ \rho_w(862)$

907

908

909 Table 5. Statistics of the quantitative C_{SPM} retrieval algorithms using their original empirical
910 coefficients.

		Novoa_17	Dogliotti_15	Han_16	Mao_12	GOCI	Shen_10	Dsa_07	Gohin_05	He_13	Doxaran_02
All (N = 437)	Slope	0.73	1.17	0.46	0.00	34.34	1.08	NA	NA	NA	NA
	R^2	0.78	0.80	0.65	0.52	0.79	0.78	NA	NA	NA	NA
	rMAD (%)	78.6	55.1	62.7	290.5	1159.7	168.5	NA	NA	NA	NA
	RMSD	191.8	204.6	273.4	427.5	13771.7	196.8	NA	NA	NA	NA
SPM < 50 mg/L (N = 214)	Slope	1.58	2.10	1.76	0.04	12.76	12.48	5.85	2.32	NA	NA
	R^2	0.53	0.44	0.40	0.50	0.03	0.13	0.66	0.07	NA	NA
	rMAD (%)	114.3	64.5	77.9	479.5	140.8	290.3	1921.9	277.63	NA	NA
	RMSD	10.5	14.9	12.7	9.3	116.5	114.0	67.2	9.91	NA	NA
SPM > 50 mg/L (N = 223)	Slope	0.70	1.16	0.41	0.00	36.93	1.04	NA	NA	1.83	0.96
	R^2	0.69	0.72	0.50	0.35	0.74	0.74	NA	NA	0.80	0.83
	rMAD (%)	41.3	45.3	46.9	93.6	2221.5	41.6	NA	NA	79.8	36.9
	RMSD	273.8	292.0	390.5	610.9	19679.5	256.1	NA	NA	534.3	218.0

911 * NA indicates no information available or not applicable.

912

913 Table 6. Statistics of the derived C_{SPM} by quantitative C_{SPM} retrieval algorithms with recalibrated
914 empirical coefficients using the four *in situ* datasets of this study.

		This Study	Novoa_17	Dogliotti_15	Han_16	Mao_12	GOCI	Shen_10	Dsa_07	He_13	Doxaran_02
All (N = 437)	Slope	0.91	0.92	0.74	0.84	1.00	0.87	0.91	NA	NA	NA
	R^2	0.91	0.80	0.80	0.67	0.79	0.90	0.82	NA	NA	NA
	rMAD (%)	41.3	76.2	44.6	61.2	64.6	46.3	42.5	NA	NA	NA
	RMSD	122.0	171.8	183.8	219.6	183.4	128.6	162.8	NA	NA	NA
	OWR (%)	57.9	48.9	58.0	46.7	29.0	52.7	56.8	NA	NA	NA
SPM < 50 mg/L (N = 214)	Slope	0.97	1.11	1.38	1.87	0.26	0.46	0.60	1.13	NA	NA
	R^2	0.59	0.55	0.46	0.27	0.36	0.17	0.51	0.52	NA	NA
	rMAD (%)	50.0	102.9	56.3	60.0	67.5	59.6	52.1	53.3	NA	NA
	RMSD	6.5	7.2	9.4	14.7	9.5	9.3	7.1	7.9	NA	NA
	OWR (%)	57.3	48.3	52.7	57.6	27.7	50.2	46.7	46.4	NA	NA
SPM > 50 mg/L (N = 223)	Slope	0.94	0.93	0.72	0.80	1.07	0.89	0.87	NA	0.77	1.00
	R^2	0.88	0.72	0.72	0.53	0.74	0.87	0.74	NA	0.80	0.85
	rMAD (%)	32.2	48.3	32.4	62.4	61.7	32.4	32.6	NA	42.5	31.6
	RMSD	174.2	245.4	262.5	313.5	262.0	183.6	232.5	NA	224.2	188.4
	OWR (%)	54.4	45.7	59.6	31.6	30.0	51.9	64.7	NA	52.7	59.3

915 * NA indicates no information available or not applicable.